UNIVERSITY OF TWENTE.

Faculty of Engineering Technology

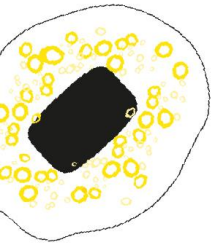

Controller design for an MR safe vane motor

Stefan Blöte S2868261
Master: Mechanical engineering(Specialization Robotics)
Daily Supervisor: dr.ir. W.B.J. Hakvoort
Internal examiner: dr. J. Dasdemir
External examiner: dr. A. Sadeghi

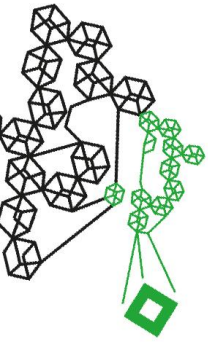

26 Januari 2024

Acknowledgement

I would like to express my gratitude to my daily supervisor dr.ir. W.B.J. Hakvoort. For his guidance and encouragement throughout the whole graduation thesis. I would also like to thank my brother Herman for his feedback and J.Mulder for making me familiar with the vane motor electronics.

Abstract

This work focuses on improving the point to point and trajectory control of a vane-type air motor. Such motors can be constructed without electrically conducting materials, making it MR-safe. However, the actuation of the vane motor through long transmission lines with inherit air compliance, in combination with worm gear friction, leads to the problem of virtual play. This presents a significant challenge for achieving optimal position accuracy. The currently used control techniques are a PD-pulse width modulation (PD-PWM) controller and a sliding mode controller (SMC). To improve control three different control techniques are proposed, including a cascade PID-PI with feedforward control, full state feedback control (FSF), and an input to output feedback linearization controller.

These three different controllers are designed within the TWINCAT3 environment for a Beckhoff PLC and evaluated in an experiment with 100 setpoints between 0° and 25000° and a simple trajectory. The results are then compared to the already implemented SMC and PD-PWM controller.

The first implemented controller was a cascade PID-PI controller with feedforward control, where the inner PI loop controlled the pressure and the outer loop controlled the position. The feedforward term was added to compensate for dynamic friction and static friction. After that, a FSF controller with integrator action was implemented. The results showed that the FSF-I controller was superior to the PID-PI-FF controller. Following this, the input-output feedback linearization method was used to decouple the input and output using the full state feedback controller. This input-output feedback linearizable controller, without the use of the proportional valve, was able to achieve a accuracy and repeatability of 4.77±38.9° and decent tracking.

The results showed that only the input-output feedback linearized controller without the proportional valve achieved superior accuracy and repeatability in setpoint control and similar trajectory control when compared to the SMC and PD-PWM controller. Still, further research is needed to improve on handling unknown disturbances and the problem of time delay.

Contents

List of abbreviations

CM	Control module
VM	Vane motor
NPS	Needle positioning system
MR	Magnetic resonance
CPR	Counts per rotation
SMC	Sliding mode control
FRF	Frequency response function
RMS	Root mean square
PWM	Pulse width modulation
IOFL	Input to output feedback linearization
ω_c	Crossover frequency

1. Introduction

This chapter provides background information on the research and reviews the literature on different types of controls for a vane type motors. Next, the main control challenges are stated and the different control methods are proposed. Finally, the outline of the research is presented.

1.1. Background

The use of image guidance for needle insertion through the skin is an new approach for biopsies or ablation. These minimally invasive interventions offer great benefits such as less tissue damage and quicker recovery. The success of these interventions is partially dependent on the correct positioning of the needle tip with millimeter precision. Earlier minimally invasive surgeries where conducted with manual needle placement. To improve needle placement the Faculty of Engineering Technology at the University of Twente and DEMCON have developed a needle positioning system (NPS) [1]. This system was designed to improve needle placement using image guidance with a CT scanner.

To increase usability, an MR-safe variant was developed by J. Mulder [2], as depicted in Figure 2. This MR-safe variant has no metal components and uses a vane-type air motor, as depicted in Figure 1. This type of motor utilizes vanes, as its name suggests. These vanes are deployed when a pressure differential arises across them. This, in turn, leads to the rotation of the rotor, generating continuous power.

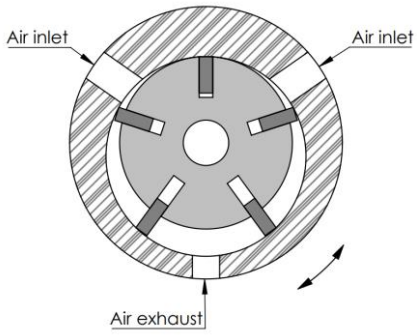

Figure 1. Schematic of the vane motor (VM)

The required air for the vane motor is supplied through long transmission lines, which results in control challenges such as air compressibility in combination with worm gear friction, which leads to the problem of virtual play. Also, the elimination of all metal components resulted in a design with lower inertia and less stiffness making it even harder to control. Designing adequate control requires a sufficiently accurate model of the MR-safe vane motor, which was developed by A. Vogelzang [3]. The main theme of this report is to enhance the accuracy and repeatability of the MR-safe vane motor for both point-to-point and trajectory control. This requires further research on the control of the MR-safe vane motor and the tuning process of the controller.

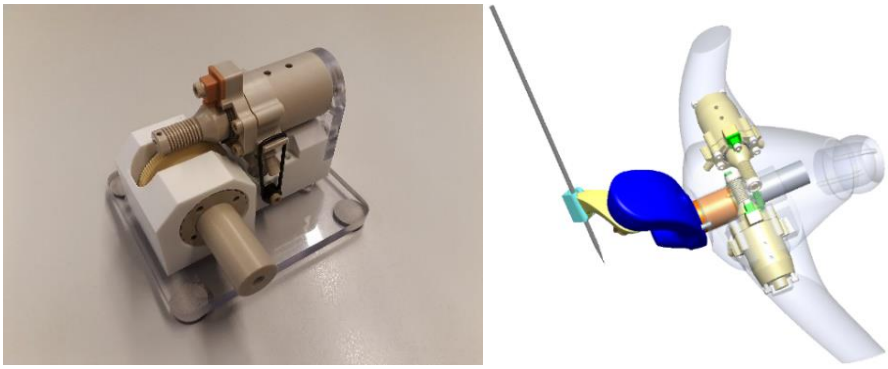

Figure 2. A schematic overview of the NPS (right) with two vane motors (yellow) and the vane motor (left), image adopted from [2].

The necessary air pressure to actuate the vane motor is supplied by the control module (CM), which is placed outside the MRI scanners environment. This CM is visible in Figure 3 along with the schematic of the pneumatic system. A proportional servo valve is used to control the mass flow of air (II). The direction of this flow is controlled with two fast switching directional valves (III). The air pressure is then measured with a pressure sensor and continues to flow through a 5 meter long tube (IV) to the vane motor (V). Another directional valve activates (VI)) a pretension mechanism (VII), which increases the friction and stiffness to reduce backlash and making point-to-point control more accurate.

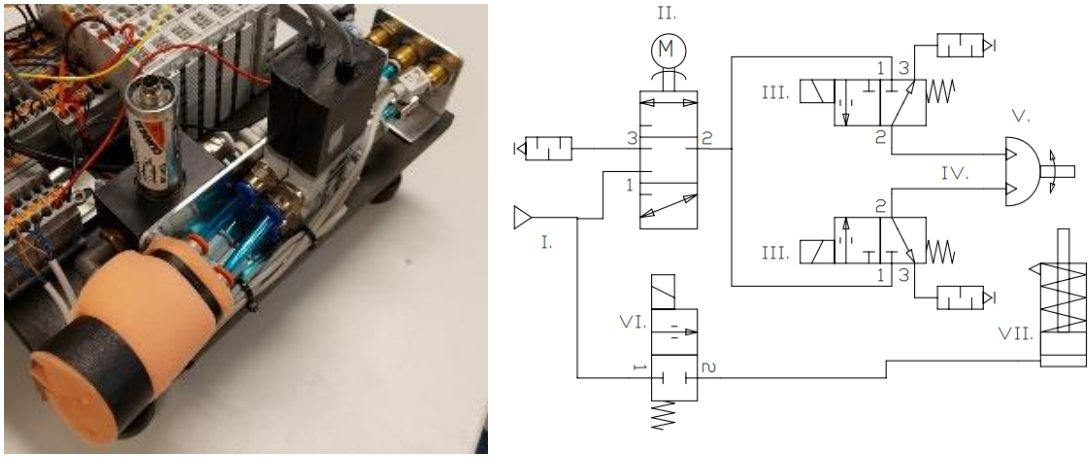

Figure 3. Control module (left) and the pneumatic flow schematic (right) with (I) pressure source,(II) proportional valve, (III) 2x fast switching directional valves, (IV) 5m tubes, (V) MR-safe vane motor, (VI) pretension valve, (VII) MR safe pretension switch. Image adopted from [2].

Different control schemes have been applied to the MR-safe type-vane motor. Initially, a PID controller was used, but it resulted in overshooting the setpoint repeatedly, which was caused by hunting movement. Even when only PD control with pulse width modulation (PD-PWM) was used, oscillation could not be eliminated. This hunting behavior around the setpoint, caused by the combination of the air compliance of the long tubes and the static worm gear friction is one of the main challenges for controlling this VM. To address this issue, a sliding mode controller (SMC) was implemented, which decreases the sensitivity to hunting. All of the sensors and actuators are connected to a Beckhoff PLC that is programmable using the TwinCAT3 environment.

1.2. Literature review

The goal of this literature is to establish an overview of existing controllers for pneumatic actuation systems, and with this overview find a suitable controller for the vane-motor. The used method involved a literature search on Scopus using the keywords “vane motor control” , “control Pneumatic actuator” , and “Time delay control pneumatic actuators” resulted in a collection of 15 papers. In this section only the most relevant papers on control of the vane motor type actuators, and pneumatic actuators with long transmission lines are discussed. The rest can be found in Appendix A: Overview Literature study.

Various techniques to control vane motor type actuators are mentioned in the literature, these include: PI/PID, sliding mode, multiple sliding surfaces controllers, dynamic surface control. In recent years actuator systems are designed with intelligent control or adaptive control, such as NN-based control or cascading control which uses both position and velocity. Some controllers make use of disturbance observer based feedback to deal with disturbance/uncertainties of pneumatic systems. The found control techniques are sorted in linear/non-linear groups.

Linear control

Linear control techniques, such as PI (Proportional-Integral) and PID (Proportional-Integral-Derivative) controllers, have found wide application in the control vane type actuators. The control schemes in found papers are illustrated in Figure 4.

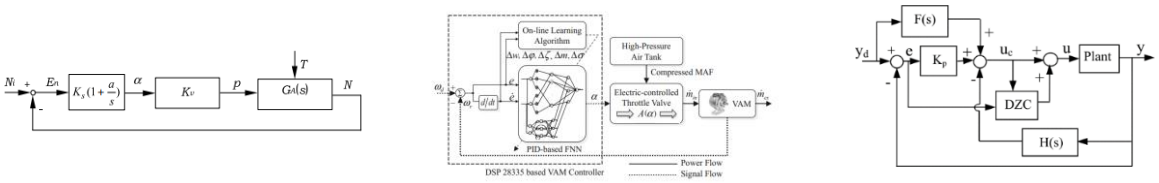

(a) Zhang et al. Adapted from [4]

(b) Yi chen et al. Adapted from [5]

(c) Ning et al. Adapted from [6]

Figure 4. Linear control schemes

In the field of rotary-type air motors, early implementations of PI controllers were explored by Zhang et al [4] . This particular study employed a model-based approach using a PI controller to regulate position and velocity. However, this study did not consider delays, uncertainties, or disturbances.

Yi chen et al. [5], proposes a model free approach were a fuzzy neural network (FNN) is used to tune the PID control parameters for a vane-type motor. An improvement in speed tracking was seen when compared to normal PID, also the proposed FNN-PID controller was more robust.

Lastly, a study from Ning et al. [6] presented a controller known as Position plus Velocity plus Acceleration feedback combined with feedforward and dead zone compensation (PVA+FF+DZC). It was compared with a nonlinear sliding mode controller, and the results demonstrated the superiority of the sliding mode controller over the PVA+FF+DZC method.

Non-linear control

Nonlinear control techniques are better suited for controlling the vane-motor due to its strong nonlinear dynamics. However, these techniques have increased complexity. Examples of nonlinear control techniques include feedback linearization, backstepping, and sliding mode control(SMC). The control schemes of relevant papers are presented in Figure 5.

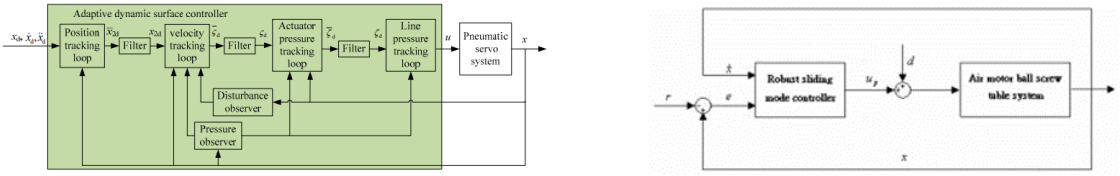

(a) Meng et al. Adapted from [7] (b) Lu et al. Adapted from [8]

Figure 5. Nonlinear control schemes

To overcome the effect of uncertainties such as leakage and friction Lu et al. [8] proposes a robust SMC design. The research results demonstrate that sliding mode control effectively handles the nonlinearities which come from air compressibility and friction.
One notable source that explored the topic of an MRI-safe controller with long transmission lines is a publication by Meng et al. [7], which proposes a pressure observer based adaptive dynamic surface controller (DSC). The pressure observer is used to predict the pressure at the inlet of the pneumatic cylinder and the long transmission lines are modeled as a nonlinear first order system. The DSC overcomes the problem of "explosion of complexity", which is often seen in techniques such a backstepping control. The results confirmed that the controller had good tracking performance and was robust to sudden disturbances.

Discussion

An overview of different control techniques for pneumatic vane control has been presented, with a summary of all the identified papers in Appendix A: Overview Literature study .

The implementation of PI and PID control for pneumatic actuators was found to be not as accurate as non-linear control methods, even when feedforward methods where introduced as described in [6]. Authors who adopted a cascade control structure saw improvement when compared to non-cascade structures and even better performance was acquired when some form of disturbance-observer based control was introduced to address friction and nonlinear dynamics. Unfortunately, few sources where found on vane motor control with long transmission lines. One of the major problems is to measure the pressure near the actuator, also the time delay caused by the long transmission lines is a challenge and only mentioned by [7], [9].

In conclusion, although a lot of control techniques for vane type actuators have been researched in the period 2002-2021, almost no papers researched vane motor point-to-point control with long transmission lines, which is probably due to the limited use cases for such devices. All in all it is clear that there is still room for improvement on the controller designs for these systems. From the available methods, a choice has been made to further research a cascade, non-linear and full state feedback controller.

1.3. Problem statement and contribution

Technological advances in needle insertion though the skin for biopsies or ablation, is becoming a more widespread method. A needle positing system could be beneficial for such procedures. The designed MR-safe vane motor is not yet capable of precise needle placement. The actuation of the vane motor through hoses with inherit air compliance, in combination with worm gear friction, leads to the problem of virtual play. This presents a significant challenge for achieving optimal needle placement. Therefore, improving the accuracy of the system with control methods will be the main purpose of this research. The following research question was formulated:

- Can improvements be made for the point-to-point and trajectory control for an MR safe vane motor?

The project aims to make the following contributions to improve the control:

- Implementing and evaluate a Feedforward-PI-PID cascade controller to control pressure first and with the pressure a position.
- Implementing and evaluate a full state feedback controller
- Implementing and evaluate a nonlinear based feedback controller which can handle static friction and delay in the hose.

These three controllers are identified as relevant control techniques, as found in the literature chapter 1.2. Additionally, the chosen relevant controllers are compared to the already implemented PD-PWM and SMC controllers. Furthermore, the system has some non-linearities, and not all states are being measured yet. To address these issues, some contributions on improving the optical encoder of the vane motor and characterizing the worm gear friction and model it for online identification are made also.

1.4. Outline

First, the system model is introduced, where the general assumptions and the non-linear dynamics of the system are explained. Next, the system identification and parameter estimation are explained, and also the need for a linearized system. After that , the method and used metrics for quantitative evaluation of the control techniques are explained. Furthermore, the research with full state feedback and feedforward cascade PI-PID on the vane motor is presented and discussed. The next part considers a nonlinear input-to-output feedback linearizable controller. In the final chapter, conclusions regarding the new controllers compared with the old controller are made, and some recommendations for future work are stated.

2. system description

This chapter first describes the experimental setup of the vane motor. After this description , the chapter continues with an explanation of the van motor model. The plant model is essential for the analysis and design of the control system in this report. After that the parameter estimation is described. Lastly, the methods used to evaluate the performance of the system are explained.

2.1. Experimental setup

This section first describes the important hardware of the setup, after that the changes of the system designed by J.Mulder [2] are described.

The first component is a pressure source which is an compressor. The proportional valve (II) in Figure 3 is the Camozzi LRWA0-34-2-A-10 which controls the mass flow and two Festo MHE3-MS1H-3/2G-M7-K fast switching valves (III) for controlling the flow direction. The pressure at the CM is measured with a two PSE540-M5 pressure sensors. The vane motor uses an incremental optical encoder with remote electronics as designed by [10]. The used fiber optic transmitter and receiver are two integrated fiber opt click boards. The existing encoder disc was 3D printed and had a resolution of 20 counts per rotation (CPR), which resulted in an output shaft resolution of 0.045°.

As part of this work the resolution of this encoder disc was improved, as depicted in Figure 6. The choice of a 50 CPR encoder disc guaranteed a 90° phase difference between the two encoder signals. The result was a resolution of 0.018°.

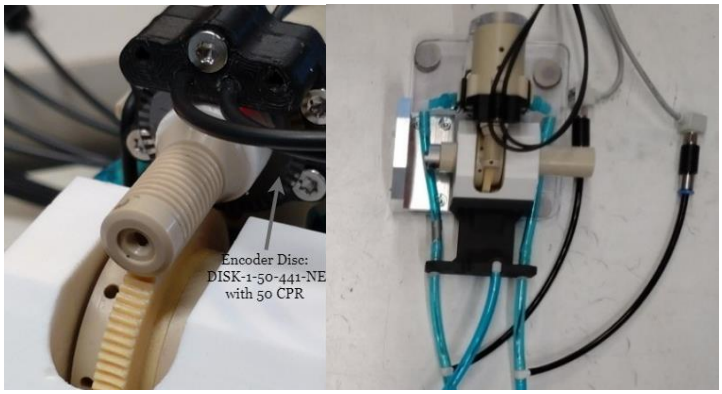

Figure 6 Encoder with improved encoder disc (left), measurement setup for obtaining the required pressures at the VM inlet (right)

To apply control techniques such as full state feedback, it is required to obtain the vane motor inlet pressure. However, the pressure at the inlet cannot be measured directly due to the MR-safe requirement. Two alternatives were considered: using an observer to estimate the VM inlet pressure, or feeding back air from the VM inlet back to the control module through small tubes. The last option was chosen, which involves a small 4 mm tube for each direction , two T-junctions, and two PSE540-M5 pressure sensors, as shown in Figure 6. Unfortunately, the addition of a T-junction and an extra tube adds an additional pressure drop which influence the mass flow to the VM. Additionally, the extra time delay between (15-20) ms of the long feedback line only influence the pressure measurement, which is not modeled and could influence performance. Also, adding more tubes to the already bulky tubing may not fit inside the NPS.

2.2. General assumptions

The main goal of the system model is to get insight in the VM and CM, and model a valve pressure to a rotation model of the VM, which is already designed by A. Vogelzang [3] and valid between a frequency range of 3-13 Hz.

Limiting the complexity of the model is advantageous for reducing the number of parameters, thereby simplifying parameter fitting and reducing computational load. The dynamic system behavior of the vane motor, as described by A. Vogelzang [3], is simplified. The main assumptions here include a model with ideal gas and negligible temperature effects. Additionally, only subsonic flow is considered.

Four state variables are identified as most relevant to describe the system these are the position, velocity, and the pressures at the control module (CM) and the vane motor (VM). The position and velocity are critical for the control. Additionally, the pressure drop and time delay of the long transmission lines can be described with pressures at the CM and VM. The input is the voltage over the proportional valve. Since the model has only one relevant position output, it is classified as SISO.

2.3. General equations

The model assumes that the air is ideal in all cases, therefore the ideal gas law can be used

$$p = \frac{RT}{M}\rho, \tag{2.1}$$

where p is the pressure, R is the ideal gas constant, T the absolute temperature, and M the molar mass. The differential equation based on the preservation of mass is defined as

$$\frac{dp}{dt} = \frac{p}{\rho V}(\dot{m}_{lin} + \dot{m}_{lout}), \tag{2.2}$$

with $\dot{m}_{lin}$ and $\dot{m}_{lout}$ being the inlet and outlet mass flows. The effect of change of mass due to changes in temperature are neglected.

2.4. Line resistance

The line is modeled as one resistance, where the volumes are divided between both sides of the line. The modeled pressure drop is

$$p_{lin} - p_{lout} = \left(\frac{\dot{m}_{lin}}{A_p}\right)^2 \left(\frac{1}{\rho_{lout}} - \frac{1}{\rho_{lin}}\right) + \Delta p_{tur}, \tag{2.3}$$

where the pressure drop is modeled with viscous friction and momentum flux [11]. The momentum flux describes the magnitude and direction of the mass flow and is calculated with $\dot{m}_{lin}$ divided by the internal cross sectional area of the line A_p. The densities of the inlet and outlet of the line are defined as ρ_{lin} and ρ_{lout}. The viscous friction loss over the whole line Δp_{tur} is calculated as

$$\Delta p_{tur} = f_{d_{lin}} \frac{\dot{m}_{lin} * |\dot{m}_{lin}|}{2\rho_{lout} D_h A_l^2} * \frac{L + L_{eqv}}{2}, \tag{2.4}$$

with L being the length of the line and L_{eqv} the equivalent length for compensation of additional resistance caused by the curved sections in the line and D_h is the hydraulic dimeter which is identical the actual line diameter.

Also, $f_{d_{lin}}$ is a darcy number for turbulent flow only, which was verified with checking the Reynolds number in the line during testing and is calculated with the following equation

$$f_{d_{lin}} = \left(-1.8\, log\left(\frac{6.9}{Re_{lin}} + \left(\frac{\varepsilon_{rough}}{3.7D_h}\right)^{1.11}\right)\right)^{-2}, \quad 2.5$$

where Re is the Reynolds number and ε_{rough} the surface roughness of the line.
Combining equations *2.3*, and *2.4* results in mass flow in the line and can be rewritten as

$$\dot{m}_{lin} = \sqrt{\frac{(p_{lin} - p_{lout})A_l^2}{\frac{1}{\rho_{lout}} - \frac{1}{\rho_{lin}} + f_{d_{lin}}\frac{L + L_{eqv}}{4\rho_{lout}D_h}}}. \quad 2.6$$

2.5. Valve dynamics

The dynamics for the proportional valve are modeled with a discharge coefficient C_d. This number is the relationship between the theoretical mass flow where the assumption is that no energy is lost and experimental mass flow is described as

$$C_d = \frac{\dot{m}_{exp}}{\dot{m}_{theo}} = \frac{\dot{m}_{exp}}{\dot{V}\rho} = \frac{\dot{m}_{exp}}{A\sqrt{2\rho\Delta p}}, \quad 2.7$$

where the theoretical mass flow is defined as the flow speed $\dot{V}$ times the density of the air at the valve. The difference between the two gives a value for the resistance of the valve. This equation is then used to calculate the mass flow as

$$\dot{m}_{vin} = C_d A\sqrt{2\rho\Delta p}C_f. \quad 2.8$$

In Figure 7 the control factor Cf is modeled to relate the input voltage over the proportional valve to a mass flow. The relation between the two is derived from the proportional valves manufacturers data as mentioned by A. Vogelzang [3].

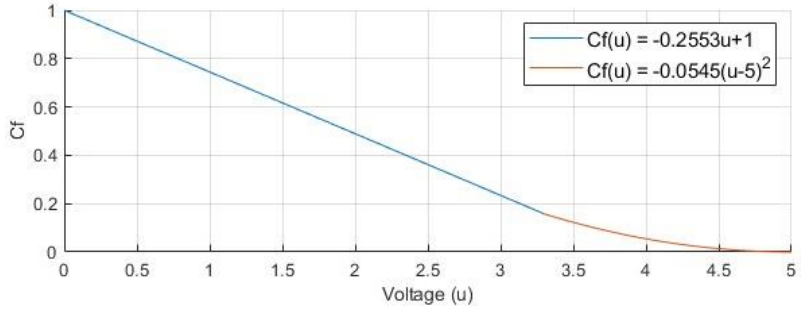

Figure 7 Relation between the Control factor and Input voltage [12]

2.6. Vane motor dynamics

The torque from the vane motor is generated though an absolute pressure difference with the environment and D_{ia}, which is a averaged value of the surface area of the passing vanes, as depicted in Figure 8.

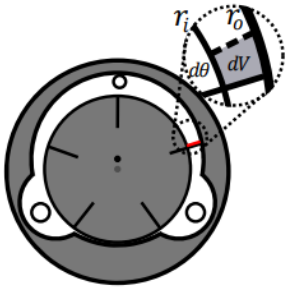

Figure 8, an impression of the vane motor with the red line showing $D_{ia}(\theta)$, image adopted from A. Vogelzang [3]

The used friction model is defined as

$$p_{fric} = sgn(\dot{\theta})\left(f_{offset} - f_{dyn1}(\dot{\theta}) - f_{dyn2}\left(\dot{\theta}^2\right)\right), \tag{2.9}$$

with f_{offset} being the offset coefficient and f_{dyn1} and f_{dyn2} being the viscous and drag friction coefficients. The vane model with viscous friction is defined as

$$I\ddot{\theta} = \left(p_{in} - p_{fric}\right)D_{ia}, \tag{2.10}$$

where the moment of inertia of the vane motor is given by I.

2.7. System model

With the general equations in section 2.3 and combining all of the valve, line, and vane motor dynamics, the state space equations for the system becomes

$$\begin{cases} \dot{x}_1 = x_2 \\ \dot{x}_2 = \dfrac{\left(x_3 - sgn(x_2)\left(f_{offset} - f_{dyn1}x_2 - f_{dyn2}x_2^2\right)\right)D_{ia}}{I} \\ \dot{x}_3 = \dfrac{x_3}{V_l\rho_{x3}}\left(\sqrt{\dfrac{(x_4 - x_3)A_p^2}{\dfrac{1}{\rho_{x_3}} - \dfrac{1}{\rho_{x_4}} + f_d\dfrac{L + L_{eqv}}{4\rho_{x_3}D_h}}} - x_3C_{loss} - \rho_{x_3}x_2D_{ia}\right) \\ \dot{x}_4 = \dfrac{x_4}{V_{valve}\rho_{x4}}\left(C_dA_v\rho_{x4}\sqrt{\dfrac{2(p_{in} - x_4)}{\rho_{x4}}}C_f - \sqrt{\dfrac{(x_4 - x_3)A_p^2}{\dfrac{1}{\rho_{x_3}} - \dfrac{1}{\rho_{x_4}} + f_d\dfrac{L + L_{eqv}}{4\rho_{x_3}D_h}}}\right). \end{cases} \quad (2.11)$$

The state vector is described as $x = [x_1\ x_2\ x_3\ x_4], x_1 = \theta, x_2 = \dot{\theta}, x_3 = p_{lout}, x_4 = p_{lin}$. The outlet pressure of the line x_3 is directly fed into the vane motor, a term for mass flow losses is incorporated in $\dot{x}_3$ as seen in equation 2.11. All of the required pressure are relative. Furthermore, a description of the system parameters are given in Table 1.

Table 1 Descriptions of system parameters

Parameters	Description
$f_{offset}[Pa]$,$f_{dyn1}[\frac{Pa}{rad/s}]$, $f_{dyn2}\ [\frac{Pa}{rad/s^2}]$	Offset, dynamic, and drag friction coefficients
$I\ [kgm^2]$	Moment of inertia of the vane motor
$D_{ia}\ [m^2]$	Averaged vane volume change
$A_p, A_v[m^2]$	Inner surface area of the line and valve
$V_l, V_{valve}[m^3]$	Lumbed volumes of the line and valve.
$D_h\ [m^2]$	Hydraulic diameter of the line, same as the line diameter.
$L_{eqv}\ [m]$	Equivalent length of the line
$f_d(\dot{m}_l)\ [-]$	Darcy number
$C_f(u)\ [-]$	Control factor
$C_{loss}(p)\ [\frac{kg/s}{Pa}]$	Mass loss factor
$\rho\ [\frac{kg}{m^3}]$	Density of the air
$p_{in}\ [Pa]$	Source pressure of the system

2.8. Control implementation

The general approach for designing and implementing a controller was to first make it work in MATLAB/SIMULINK on the 4_{th} order model as described in section 2.7 and then rewrite the code manual to the TWINCAT3 environment. Unfortunately, it was not possible to realize code generation from the model using Simulink real time or any other interface package provided by Beckhoff due to license issues.

2.9. Verification method

The performance of the controller design is evaluated though the use of five different metrics, as given in Table 2.

Table 2 definition of metrics

Metric	**Definition**
Position error (°)	$e_{pos} = x_1 - setpoint$, where x_1 is the steady state position.
RMS (°)	Root mean square defined as: $RMS = \sqrt{\frac{1}{100}(e_1^2 + e_2^2 + .. + e_{100}^2}$
Overshoot (%)	Percentage of the maximum peak value of the response compared to the setpoint.
Settling time (s)	Time required to stay within a range of $\pm 250°$ of the setpoint.
Rise time avg(s)	Time required to reach 90% of the setpoint height.
Hunting bandwidth (°)	The peak value of the oscillating movement around a setpoint. Often not relevant because the controller shuts down if a specified bandwidth is reached.

The point-to-point control is evaluated in an experiment with a fixed setpoint set of 100 random points between 0° and 25000° on the output axis, the results are then compared with the performance of a PD-pulse width modulation (PD-PWM) controller and a Sliding mode controller (SMC) as provided by J.Mulder [2].

Besides point-point control trajectory control is considered. This is relevant for needle insertion while the patient is breathing. The scenario of needle insertion in the abdominal region of a slow-breathing person is used to define the trajectory. Slow breathing is defined as having a breathing frequency lower than 0.2 Hz [13]. This value is converted to a trapezoidal shaped trajectory with a really slow breathing period of 25 seconds with the parameters specified in Table 3.

Table 3 Trajectory parameters

Position setpoints (°)	Velocity Max ($°/s$)	Acceleration ($°/s^2$)
0-12000-0	$1 * 10^3$	300

During the experiment, the vane motor pre-tension switch will not be used, for both trajectory - and setpoint control.

2.9.1. Results SMC and PD-PWM controllers

The results obtained for point-to-point control of the already implemented controllers as designed by J.Mulder [2] are given in Table 4. The results are generated through the author of this thesis. Also the tracking performances for SMC and PD controller, are depicted in Figure 9.

Table 4 setpoint control quantification (results from own experiments)

Metric	**Requirement DEMCON**	**PD PWM**	**SMC**
Position error and RMS (°)	$46\,° \pm -$	$-29 \pm 103°$	$17 \pm 92°$
Overshoot (%)	–	1.9%	5.1%
Settling time (s)	≤ 5 (s)	2.5 (*s*)	2.4(*s*)
Rise time avg(s)	–	1.34 (*s*)	1.32 (*s*)
Hunting bandwidth (°)	–	0	0

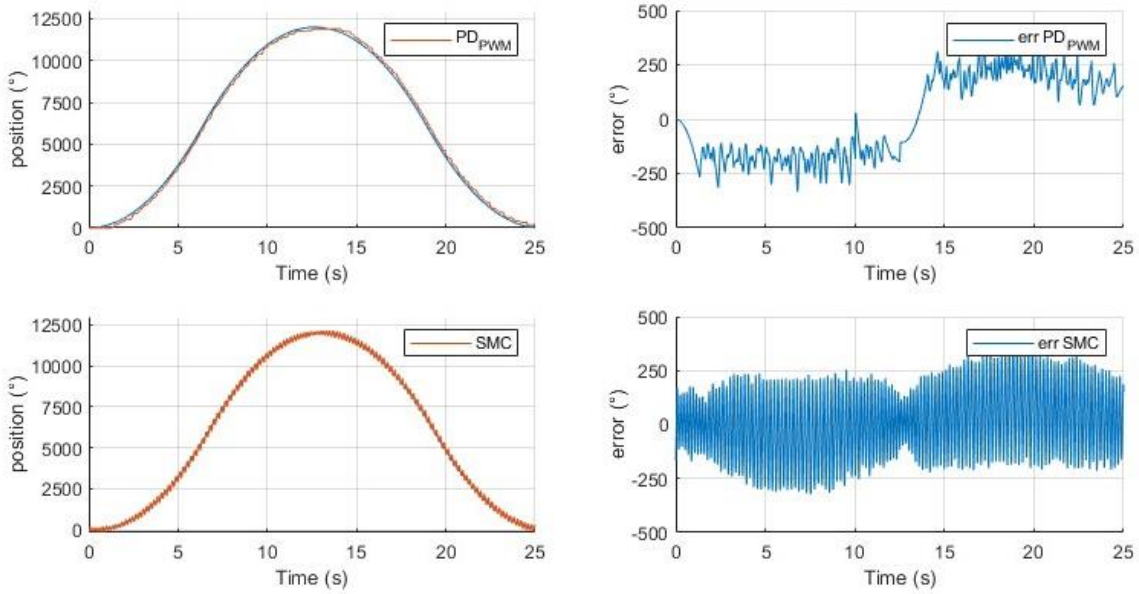

Figure 9 quantification PD-PWM(upper) and SMC(lower) trajectory experiments

2.10. System identification

This section describes how different model parameters are obtained such as: the worm gear friction coefficients, and the moment of inertia of the vane motor. Furthermore, the linearization of the model is explained and why this is desired.

2.10.1. Friction model

Various models for friction in vane motors are discussed in the literature [6], [14]. The most popular ones are either a model with Coulomb and viscous friction, or a LuGre friction model that incorporates Stribeck friction. Offline identification of the friction was obtained through an experiment where the proportional valve is gradually opened and the pressure at the VM inlet and velocity are measured. This data is then used to curve fit a function of angular velocity $p_{fric}(\omega)$. The results for the left and right valve at different inlet pressures are depicted in Figure 10, where a good correlation is seen independent of the source pressure. This data is then used to fit a Coulomb and viscous friction model with a higher order term.

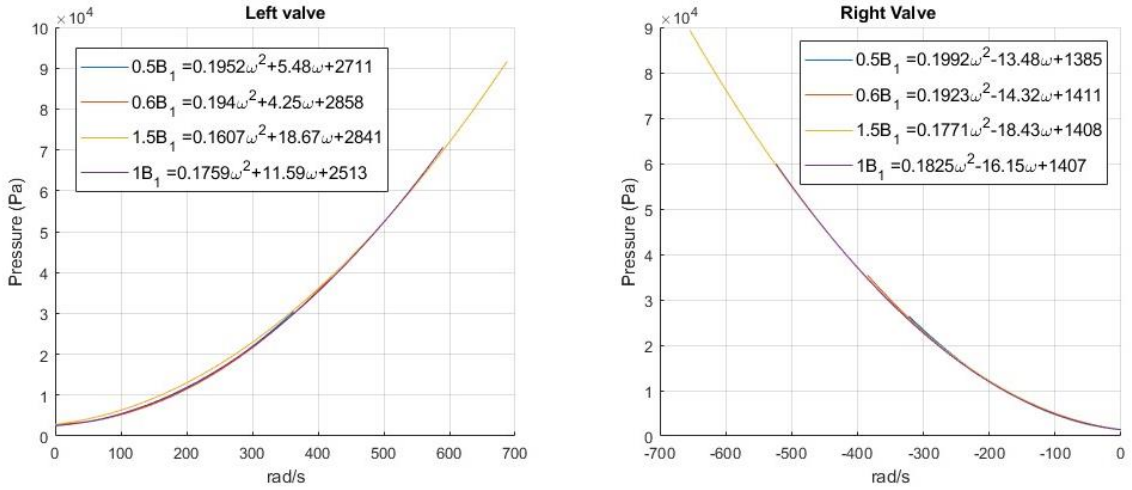

Figure 10 Friction identification of the vane motor

The results showed a severe difference between the linear - and offset term for both directions. Which made choosing the friction model parameters difficult. Additionally, it is observed that at 0.5 MPa source pressure the vane motor did not overcome the Coulomb friction between the nonlinear (3.3-5) V range. Because of this, choosing 0.5 MPa as a nominal source pressure results in no rotation of the VM in the nonlinear valve range ,which is advantageous for linearization. The proposed dynamic model for the VM is

$$\ddot{x_1} = \frac{\left(x_3 - sgn(x_2) f_{offset} - f_{dyn1} x_2 - f_{dyn2} x_2^2\right) D_{ia}}{I}, \tag{2.12}$$

where $f_{offset} = 2000\ Pa, f_{dyn1} = 14 \frac{Pa}{rad/s}$,and $f_{dyn2} = 0.18 \frac{Pa}{\left(\frac{rad}{s}\right)^2}$ are the chosen parameters.

2.10.2. Parameter estimation

The purpose of a frequency response function "FRF" is to identify the system dynamics at different frequencies. This data can then be used to estimate different model parameters and match our model. A.vogelzang [3] already made some effort to estimate parameters with a FRF via a chirp input signal. The simplification of the model and changing the friction model made some of these parameters obsolete. Redoing this parameter estimation and conducting a new FRF to get a more optimal fit of our reduced order model was necessary.

Multiple test are done using a linearly increasing chirp signal from 0 to 8 Hz over a period of 15 seconds. This signal is placed on the proportional valve with a voltage between 0-5 Volt. This chirp signal is continuously held on the proportional valve for 10 periods. Because of the directional friction as mentioned in chapter 2.10.1 each period showed a offset which made calculating a FRF hard even when detrending is used. To cope with this problem a weak P controller is used to prevent off-set. However, the use of this controller influences the system gain a bit and must be considered.

The parameters to be estimated with the FRF are only the moment of inertia I and mass flow losses. Other parameters such as the Volumes, discharge coefficient, tube roughness, and equivalent length were already determined by A.Vogelzang [3]. The moment of inertia can be found though evaluating the transfer function of

$$\frac{\theta}{\tau} = \frac{1}{Is^2 + ds}, \qquad 2.13$$

where the motor torque $\tau = \Delta P_{lout} D_{ia}$ with D_{ia} being the average vane volume change and ΔP_{lout} is the pressure differential over the vane motor. The system identification toolbox of MATLAB with the estimate transfer function model is used to fit equation 2.13 to this data, where a I of $4.47 * 10^{-7}\ kgm^2$ is calculated. The fitted transfer function is depicted in Figure 11. For reference, the calculated moment of inertia within SolidWorks is $2.26 * 10^{-7}\ kgm^2$. The difference could be explained because the pressure is measured before the vane motor constriction resulting in a larger ΔP_{lout}.

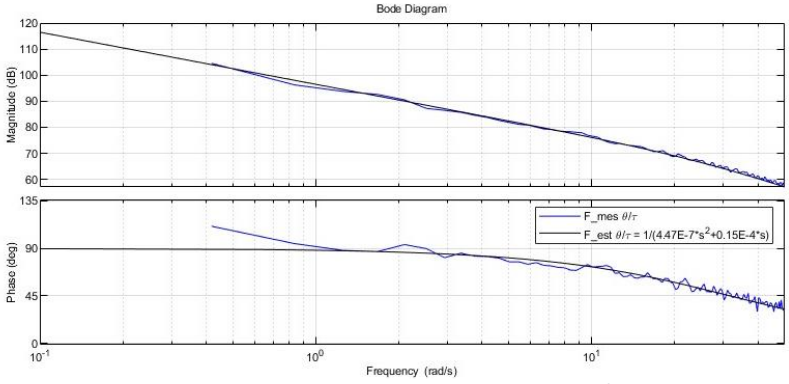

Figure 11 Frequency response of $G(s) = \frac{\theta}{\tau}$

The obtained friction functions as described below equation *2.12* are used. Furthermore, four different volumes were used in the model of A.Vogelzang [3] which are the volume of the proportional valve V_{PV}, the directional valve volume V_{DV} , the line volume V_l, and the constriction volume V_c which is volume between the VM inlet and where the line is connected to the VM. This small area has a 90° tube connection resulting in additional resistance.

The reduced order model consists only of two lumped volumes at the beginning and end of the line. So, the new volume at the beginning of the line is $V_{PV} + V_{DV}$ and the volume at the end of the line is V_l. Lastly, a constriction volume, was added by A.Vogelzang [3] to add extra resistance and to check if the air entering the VM was choking, in our case this volume is neglected.
Determining the actual leakage was the most challenging part, where increasing the C_{loss} decreases the mass flow into the VM and hereby reduces the steady state rotational speed of the vane motor. This C_{loss} was used to match the actual steady state velocity of the VM, where this value was almost a factor 10 larger than the value obtained by A.Vogelzang [3]. One reason for this could be that the constriction was neglected resulting in a higher inlet pressure on the vane motor.
The resulting FRF of the vane motor with the linearized state space representation around 1.5 V is depicted in Figure 12. The fit of the transfer function θ/u is good, only difference with the FRF is the earlier roll off near 13 rad/s. The model fit of transfer function of $Pressure/u$ shows a few dB difference in the low frequencies. One explanation could be that the added T-junction before the vane motor adds a lot of resistance. Which, resulted in a larger pressure drop over the tube. However, the obtained roll off is good.

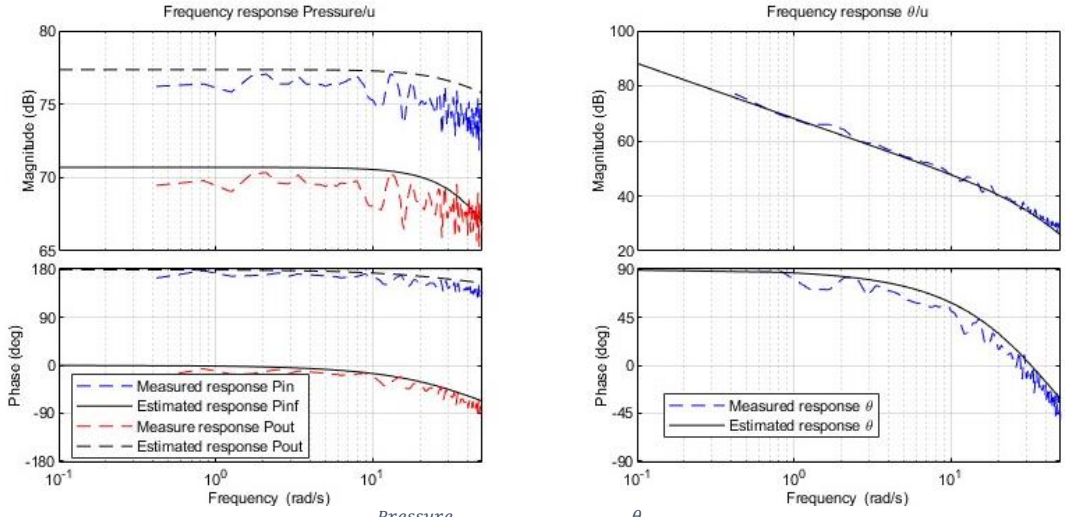

Figure 12 Frequency response $G = \frac{Pressure}{u}$ (Left) and $G = \frac{\theta}{u}$ (Right)

The fourth order model will be used for further control. Where, the new parameters are summarized in Table 5.

Table 5 estimated parameters for the fourth order VM model

Parameters	Old Value	New value
$f_{offset}[Pa]$,$f_{dyn1}[\frac{Pa}{rad/s}]$, f_{dyn2} $[\frac{Pa}{rad/s^2}]$	Only Coulomb friction model	2000,14,0.18
$I\ [kgm^2]$	$1.3 * 10^{-7}$	$4.8 * 10^{-7}$
$V_l, V_{valve}[m^3]$	-	$63 * 10^{-6}, 32 * 10^{-6}$
$C_{loss}[\frac{kg}{s}/pa]$	$3.4 * 10^{-9}$	$3 * 10^{-8}$
$D_{ia}[m^3]$	$2.508 * 10^{-7}$	$2.508 * 10^{-7}$
C_d []	0.48	0.48
$\epsilon_{rough}\ [m]$	$4 * 10^{-4}$	$4 * 10^{-4}$
$L_{eqv}\ [m]$	0.8	0.8
$L\ [m]$	5	5

2.10.3. Linearization

For linear control such as PID or full state feedback a linearized state space representation for tuning the control parameters is desired. This approximation can be used to synthesize linear controls and determine stability. Further, in a linearized system the transfer function becomes rational were the poles and zeros become defined.
The derived fourth order system has a few non linearities such as the valve – and line dynamics. The used equilibrium point for linearization is 1.5 V over the proportional valve, which is in the linear range of the valve as described in chapter 2.5. The next step involved determining the linearized state space representation with Jacobian linearization. This was achieved with the MATLAB model linearizer toolbox, the results are shown in Figure 13 with the model parameters as mentioned in Table 5.

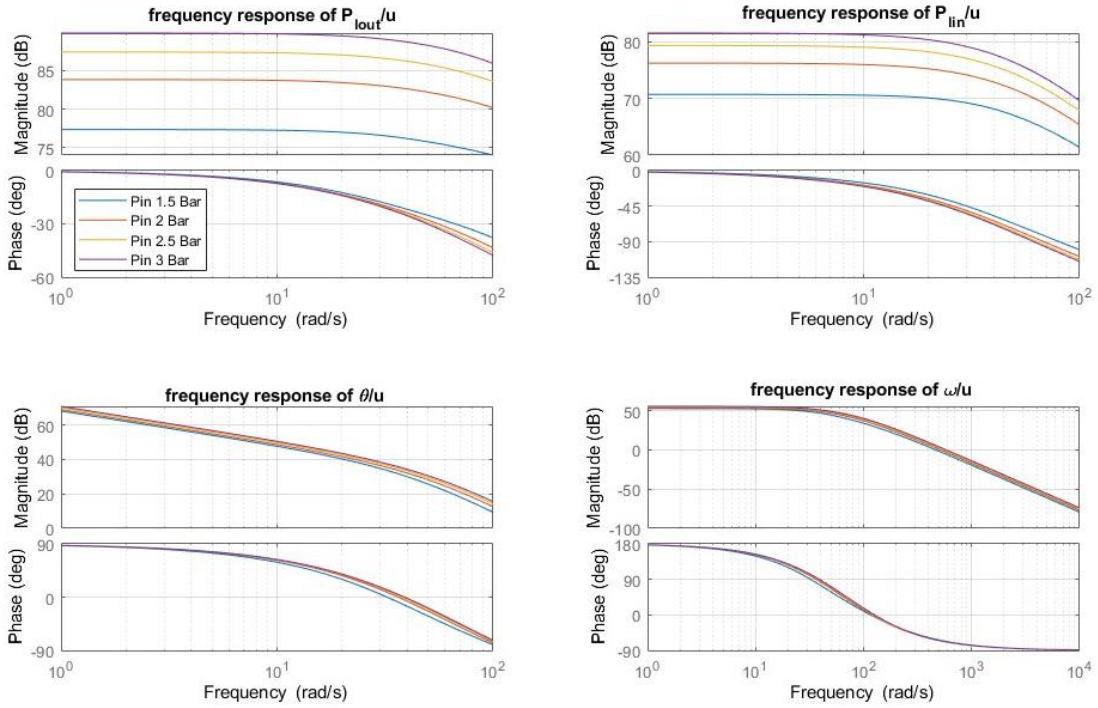

Figure 13 frequency responses of linearized state space model at different inlet pressures.

The resulting state space model could then be used for tuning the full state feedback and PID-PI-FF controller.

3. Cascade PI-PID-FF control

This chapter presents the theory and implementation of PI-PID-FF control. The following section describes the steps and challenges involved in applying this control scheme. Then, the tuning methods for the PI-PID-FF controller are explained. Finally, the results are shown and discussed.

3.1. Theory

Cascade controllers are often used in systems with multiple outputs that experience phase lag on the performance output. The simplest form of cascade control consists of an outer low-frequency controller and an inner high-frequency controller. A example of the general control structure is depicted in Figure 14, where P1 is the transfer function from $\frac{x_1}{u}$ and P2 the transfer from $\frac{x_2}{x1}$. The main purpose of this type of control is to improve the stability of the primary loop variable.

When designing these types of controllers, several points are important. First, the inner loop must respond much faster than the outer loop. A 10-fold difference in the crossover frequency ω_c between the inner and outer loop is typical seen in the literature[15]. Once the inner loop is closed, feedback control on the outer loop can be designed.

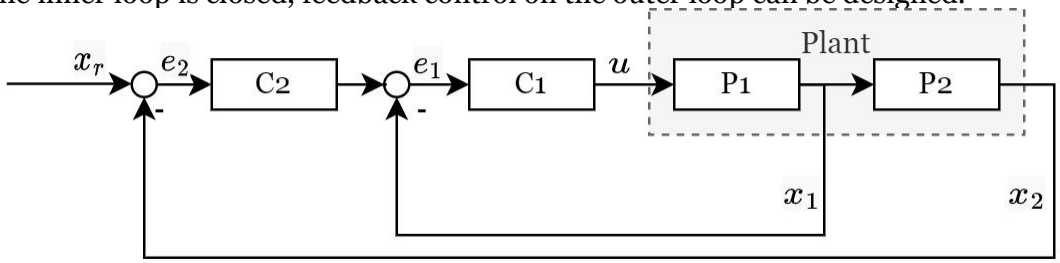

Figure 14 Generic cascade controller structure [15]

Another part of the proposed controller involves a feedforward controller. Feedforward controllers only respond to a reference control signal. Therefore, mathematical knowledge about the process is required. The benefits of using feedforward control the effect of known disturbances.

3.2. Implementation

The controller utilizes the measured pressure at the CM or VM for the inner loop and uses a PI controller, and the outer position loop uses the position data from the optical encoder where a PID controller is implemented. These are chosen based on the first and second order system behaviors observed in section 2.10. The implemented control scheme with these controllers are illustrated in Figure 15, where a reference velocity is used to determine the feedforward signal to compensate for the known friction.

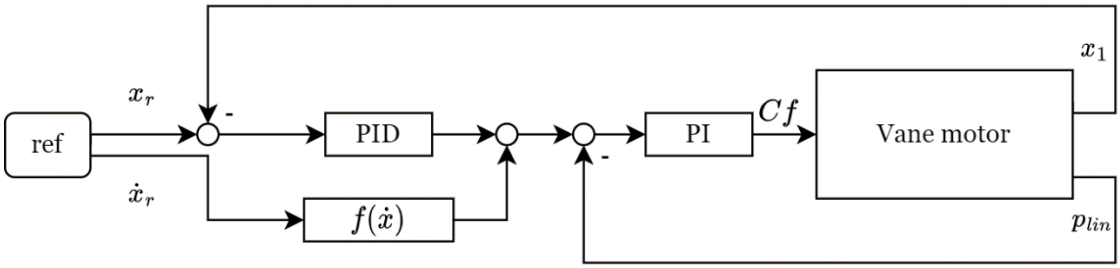

Figure 15 Control diagram of PID-PI-FF controller

Implementation requires the following actions:

- Defining a suitable gain, and cross-over frequency ω_c for inner- and outer loops.
- Tuning K_{PI}, T_i
- Tuning K_{PID}, T_i, T_v, T_d
- Determining a suitable model for the feedforward controller.

3.2.1. Feedforward

The obtained friction model as mentioned in chapter 2.10.1 describes the torque as a function of velocity

$$\tau_{fric}(x_2) = \left(-sgn(x_2)\left(f_{offset} - f_{dyn1}x_2 - f_{dyn2}x_2^2\right)\right)D_{ia}. \quad 3.1$$

Several measurement are conducted to obtain this model, which depending on the direction are forwarded to the inner loop. When done correctly, the vane motor dynamics for the PI controller should simplify to $(x_3 D_{ia})/I$. One thing that should be noted are the different friction coefficients for each rotational direction, these are not implemented in the controller. Finally, the reference velocity for point-to-point control as well as the trajectory control are determined though a setpoint generator integrated in the Beckhoff software [16].

3.2.2. PI-PID

The Inner PI loop and outer PID loop required choosing a suitable ω_c. This value was primarily dependent on actuation speed of the hardware. The Camozzi LRWA0-34-2-A-10 proportional valve has a switching time of around 7 ms from 0 thill 100 % and the 2 Festo MHE3-MS1H-3/2G-M7-K fast switching valves around 2 ms.

The frequency response of the pressure over voltages showed a bandwidth of 13 rad/s. A closer look at the pole-zero map, as depicted in Figure 16 shows a stable plant with a vibration mode at 13 rad/s. An iterative approach is used to choose the value of $\omega_{c_{in}}$ such that the linearized system in MATLAB had a rise time of the unit step response matching the actuation speed of the proportional valve. This resulted in a $\omega_{c_{in}}$ of 100 rad/s.

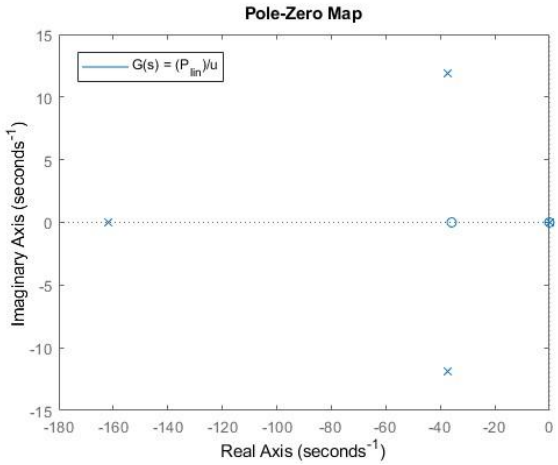

Figure 16 Pole-Zero map of the linearized vane motor at 0.5 bar inlet pressure.

For the outer loop cross over frequency ω_c had to be smaller than the inner loop. So, a $\omega_{c_{out}}$ of 8 rad/s is chosen, which guaranteed that the inner loop responds faster. How the controller gains are exactly obtained is further explained in section 3.2.3.

The implementation in TWINCAT3 used the standard PID controller blocks. To avoid integrator windup, saturation is applied, which limits the controller output within a range.

3.2.3. Parameter Tuning

PI-PID control requires the tuning of several gains. This chapter describes which procedures are followed to tune the control loops. The first procedure uses loop shaping as described in [17], this method only uses the linearized state space representation of the vane motor. Unfortunately, the obtained PID-PI parameters resulted in non-desirable system behavior. Therefore, a manual method mentioned in [18] is also adopted.

Loop shaping

The chosen bandwidths ω_c for the inner - and outer loop are 100 and 8 rad/s respectively. Furthermore, the tuning process for the pressure measurement at the CM is only described in the section. A similar approach is used for the inner loop with pressure measured at the VM.

For the PI controlled inner loop, the integrator is set to be dominant at 37 rad/s. After this frequency the phase lag is -90° and the slope -1. The gain K_p is chosen to vertically shift the frequency response of the plant to a ω_c of 100 rad/s . The step response and bode plot are depicted in Figure 17.

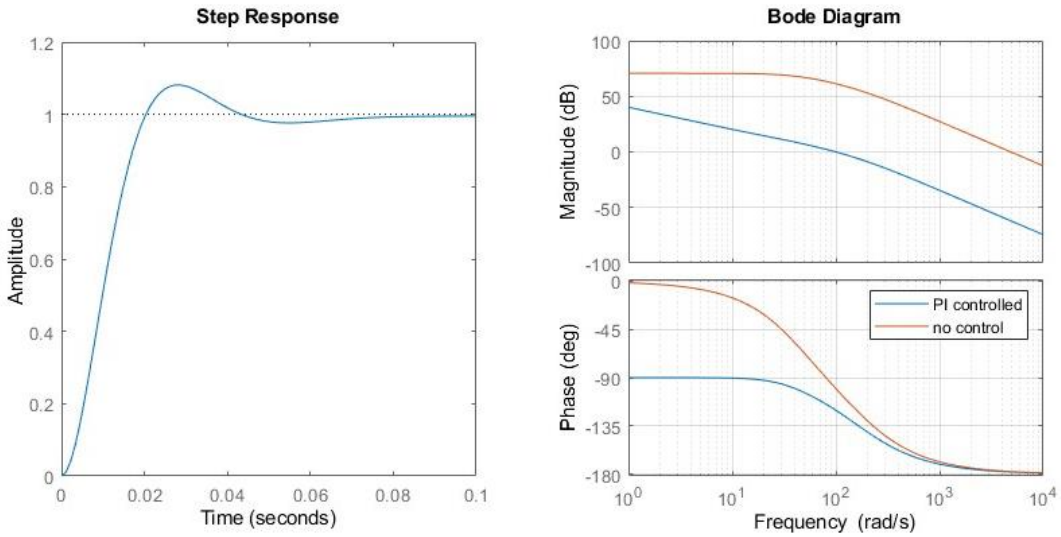

Figure 17 Frequency response of the open inner pressure loop (Right) and Step response (Left)

The simulation of the inner loop shows a unit step response with a settling time of 0.061 s and an overshoot of 8%, which is slow enough for the proportional valve to respond.

The next step involves closing the inner loop and tuning the PID control parameters. Figure 18 shows that the outer open loop crossed the 0 dB line at 0.3 rad/s, which means that it attenuated the input signal, which is not desirable. However, the gain margin is rather large and the phase margin at 8 rad/s is around 60°. The phase margin is then used to calculate the appropriate zero and pole locations. The final step is to chose K_p such that, the system magnitude crossed ω_c. The large gain margin ensured that there are no stability issues. Figure 18 depicts the resulting unit step response of the closed loop system.

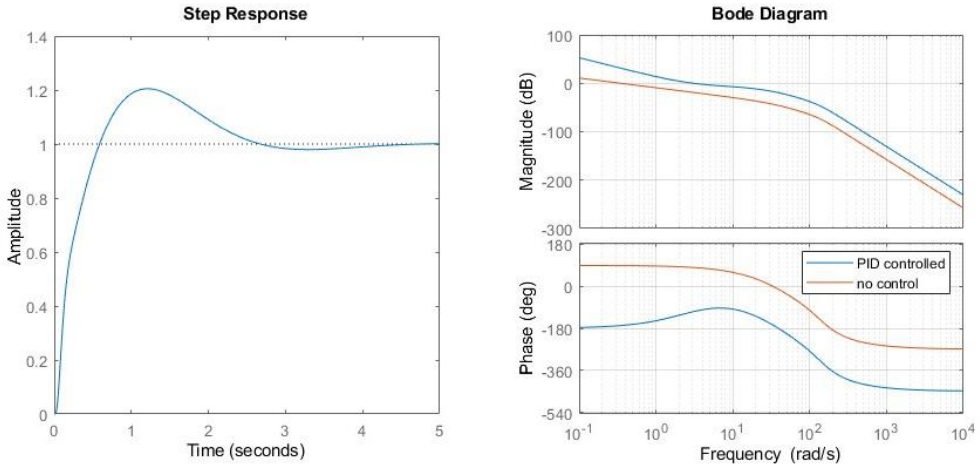

Figure 18 Frequency response of the open outer position loop (Right) and Step response (Left)

The obtained PI-PID control parameters are discretized and converted to a standard PID format

$$PID(s) = K_p\left(1 + \frac{1}{T_i s} + \frac{T_v}{1 + T_d s}\right). \quad 3.2$$

To do this two MATLAB functions where used namely : c2d and pidstd, which converts the discretized controller to standard form.

Manual tuning

For the PI controller , the first step is to determine the gain K_{PI}. This is done though setting all parameters to zero and increasing the K_{PI} value until the controlled pressure settled slightly below the desired setpoint. Next, a T_i of 100 ms is added and gradually decreased until the steady state error is minimized quickly enough.
Furthermore, the PID control parameters, where K_{PID} is chosen such that constant oscillation behavior occurred. Next the integral time T_i must be set where a large T_i is chosen and gradually decreased until a satisfactory result is obtained. Finally, the damping T_v is initially set to a very small value and is gradually increased until overshoot is minimized. The resulting parameters for both methods are given in Table 6.

Table 6 Parameters PID-PI-FF control

Parameters	Loop shaping	Manual tuning
PI-CM: K_p, T_i	$8 * 10^{-4}, 0.027$	$8 * 10^{-4}, 0.045$
PID-CM: K_p, T_i, T_v, T_d	$7.5, 1.365, 0.285, 0.035$	$725, 0.63, 0.41, 0.048$
PI-VM: K_p, T_i	$9 * 10^{-4}, 0.027$	$9 * 10^{-4}, 0.045$
PID-VM: K_p, T_i, T_v, T_d	$5.8, 1.277, 0.25, 0.041$	$750, 0.63, 0.41, 0.048$

3.3. Results

The chapter shows the results obtained from the PID-PI-FF experiments as described in chapter 2.8. Figure 19, and Figure 20 shows part of the point-to-point control with loop shaping and manually tuned parameters. Figure 21, and Figure 22 show an error plot of the tracking performance.

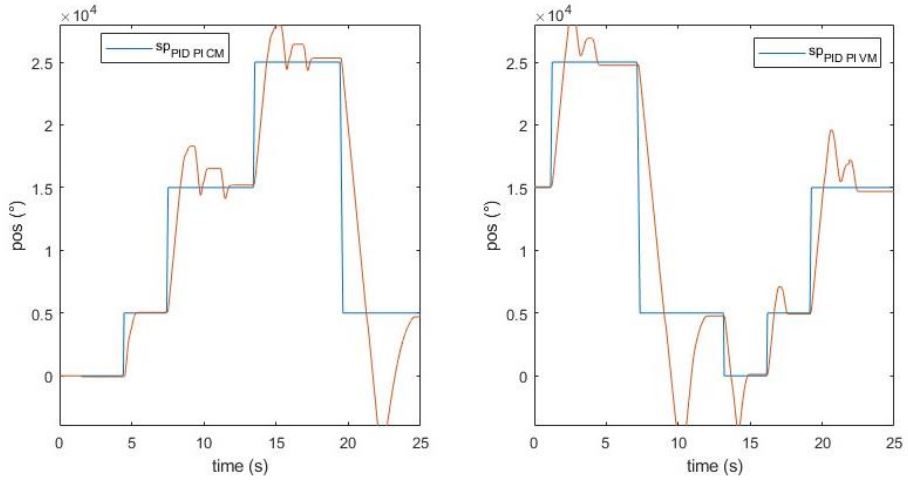

Figure 19 point-to-point control with parameters obtained though loop shaping. Shown is the pressure measurement at the CM (Left) and VM (right)

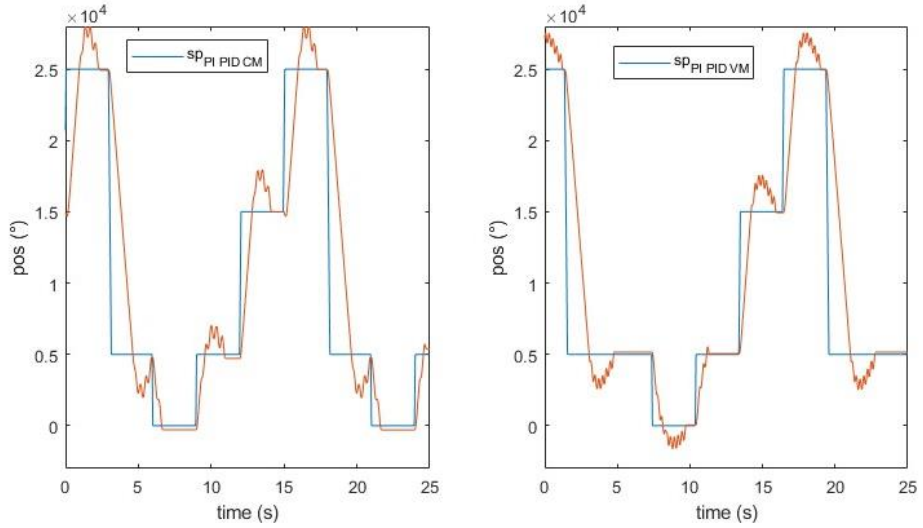

Figure 20 point-to-point control with manual obtained parameters. Shown is the pressure measurement at the CM (Left) and VM (right)

Table 7 shows some important parameters obtained from the point-to-point performance. It was observed that in some cases the vane motor did not achieve a steady position within 5 seconds the "% settling within 5 s" refers to this.

Table 7 PID-PI-FF point-to-point performance results

	Manual	Loop-shaping
	Pressure measurement at control module	
Position error and RMS (°)	$95 \pm 173.6°$	$43 \pm 215.9°$
% overshoot	22.5%	54.5%
Settling time avg (s) % settling within 5(s)	$2.3(s); 70\%$	$3(s); 73\%$
Rise time avg (s)	$0.64(s)$	$1.24(s)$
Hunting bandwidth (°)	0	0
	Pressure measurement at vane motor	
Position error and RMS (°)	$-27 \pm 81.9°$	$31 \pm 198.9°$
% overshoot	21%	39.5%
Settling time avg (s) and % settling within 5(s)	$2.5(s); 56\%$	$3.5(s); 76\%$
Rise time (s)	$0.69(s)$	$0.8(s)$
Hunting bandwidth (°)	0	0

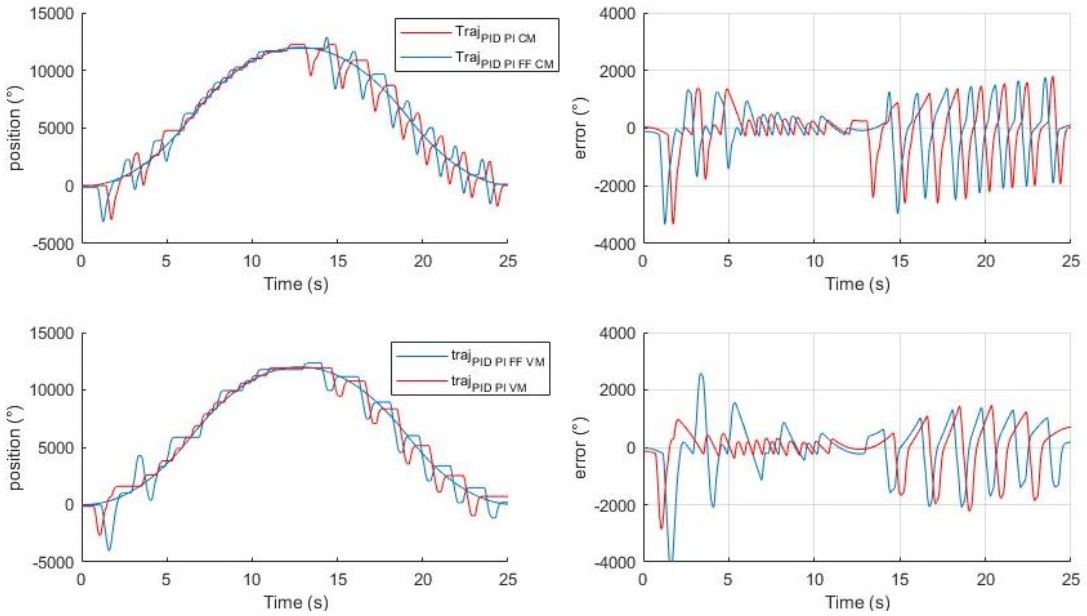

Figure 21 tracking performance (left) and reference tracking error (right) with pressure at the CM (above) and VM (below). The control parameters are obtained with loop shaping.

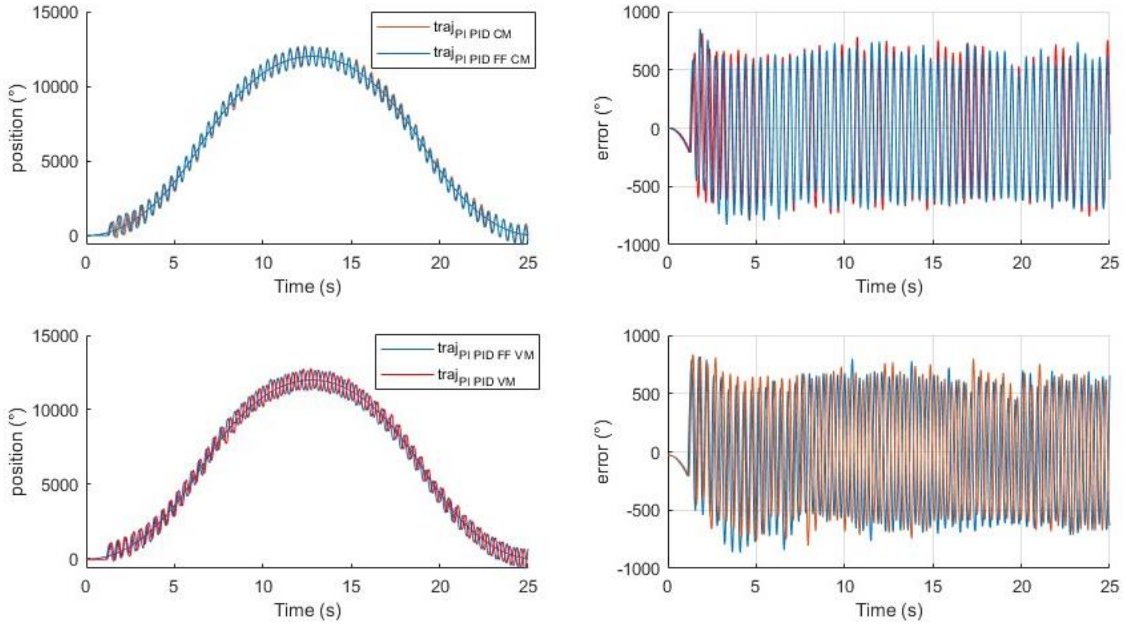

Figure 22 tracking performance (left) and reference tracking error (right) with pressure measurement at the CM (above) and VM (below). The control parameters are manual obtained.

3.4. Discussion

Figure 19 and Figure 20 show setpoint control with parameters obtained using manual and loop shaping methods. The controller that uses the pressure at the vane motor inlet performed the best in terms of accuracy and repeatability. This is unexpected since adding more time delay because of the added feedback line would typically increase the overshoot. However, a lower overshoot is observed, which may be caused by the lower integral time T_i parameter. Additionally, the actual response of the system differs from the expected unit step response, as depicted in Figure 18.

Furthermore, the manual tuned parameters showed generally better performance, as seen in Table 7. Where the inner loop controller output is not really controlling the pressure but acted more as pulse width modulation (PWM) controller. Unfortunately, none of the configuration where able to consistently settle within 5 seconds and the repeatability determined with the RMS is in all four cases large.

Regarding tracking performance, as depicted in Figure 22 and Figure 21 it is observed that really aggressive control shows superior tracking behavior with an maximum error near 720°. Interestingly, the used feedforward model did not improve the tracking behavior and in some cases made it even worse. This is probably caused by a combination of the really low inertia of the vane motor in combination with the feedforward model being the average of both rotational directions, resulting in a model mismatch for both directions.

4. Full state feedback control

This chapter explains the theory behind full state feedback. Next, the implementation is discussed including some improvements, such as the addition of a integrating action and a reference signal for the pressure. Then, the pole placement method is described. Finally, the experimental results are showed and discussed.

4.1. Theory

Full state-feedback allows to place the poles of a SISO system on any desired location using pole placement [19]. For FSF to work a state space system of the form

$$\dot{x} = Ax + Bu, \tag{4.1}$$

Is controllable if the matrix below has full row rank

$$G = [B, AB, A^2B, \dots, A^{n-1}B]. \tag{4.2}$$

The control law for FSF is

$$u = K(-x + x_{ref}), \tag{4.3}$$

where K is the feedback matrix and x the state vector. To place the poles at the desired position substitution of equation 4.3 in 4.1 is required. The resulting closed loop poles are then acquired by

$$\det|sI - (A - BK)| = 0, \tag{4.4}$$

where K is chosen such that the closed loop poles are at a desired location.

4.2. Implementation

The implemented control scheme is illustrated in Figure 23. The four different states are measured and a reference signal is also generated. The resulting position error is integrated and added as an extra state.

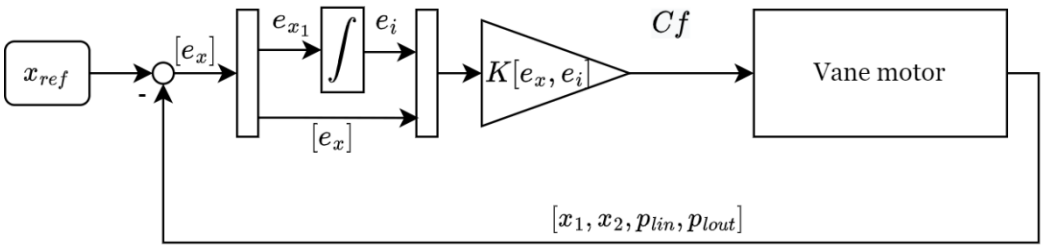

Figure 23 control scheme of FSF

Controller design of FSF requires the following steps

- Adding an extra system state for a integrating action.
- Choosing desired system poles.

And only one step is required for the implementation

- Vector multiplication of K times the state vector $x = [e_x; e_i]$.

4.2.1. Integrating action

To minimize the steady state error, an integrating action can be used to integrate the position error over time. Implementing this action requires an additional system state, the used augmented matrices are

$$\tilde{A} = \begin{bmatrix} A & 0 \\ C & 0 \end{bmatrix}; \tilde{B} = \begin{bmatrix} B \\ 0 \end{bmatrix}. \quad 4.5$$

These matrices can then be used to place an additional pole on the s plane and acquire the desired K vector.

4.2.2. Reference

First, only the position and velocity are used a reference signal. Additionally, the obtained friction model as described in section 2.10.1 is useful to create a reference for the pressures at the vane motor and control module. The resulting functions are depicted in Figure 24. These functions are used to find the reference pressures at a set reference velocity. The assumption here is that the velocity is in a steady state, and the effect of capacity is neglected

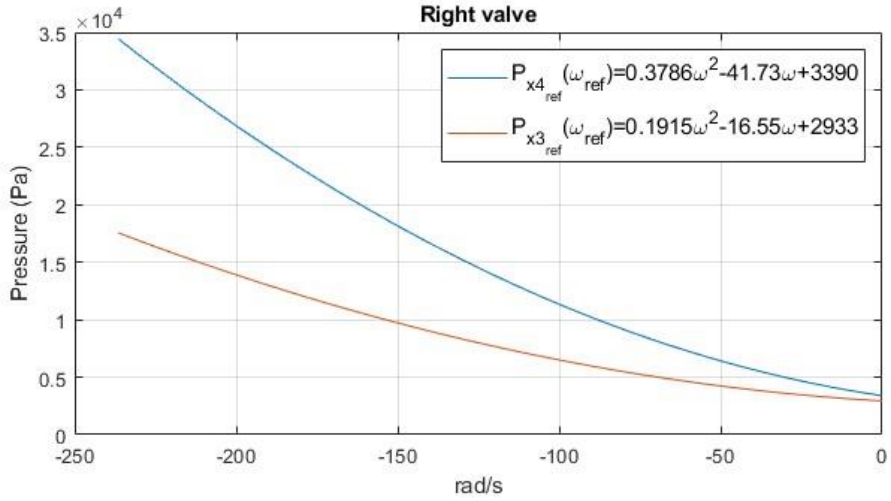

Figure 24 Trajectory references for pressure

4.2.3. Pole placement

Placing the poles at a desired location to achieve desired system behavior is done using a trial-error procedure, two different sets of poles are generated and compared. First, the poles of a fourth order Butterworth filter with a cross-over frequency of 13 rad/s showed a desirable system response. An additional fast pole at -50 for the integrating action is set manually. Furthermore, a second set of poles is generated that are comparable to the PID-PI controller poles. Placing the poles is done with the MATLAB command place() the resulting poles and zeros are illustrated in Figure 25.

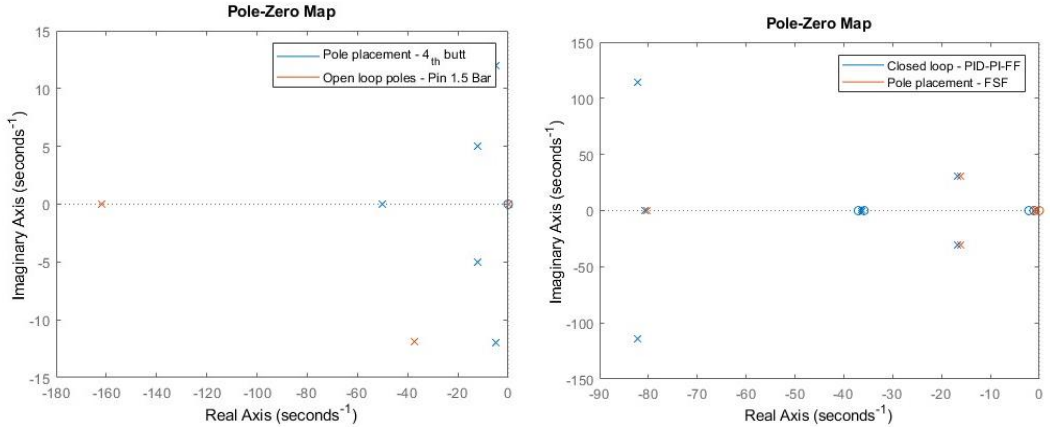

Figure 25 pole placement using Butterworth poles (left). Comparable pole placement with the PID-PI controller (Right)

The cascade PID-PI-FF controller structure adds several poles to the closed loop system. But the FSF controller can only place poles at five locations. Therefore, a tradeoff between which poles to use is required. A fast pole at -80.5 that occurred in both inner - and outer closed loop and two conjugate pole pairs at$-16.5 \pm 30i$ and $-0.74 \pm 0.74i$ are used. The slightly dampened conjugate pole pair at -38 seems to cancelled by a zero and is therefore not used.

4.3. Results

Figure 26 depicts the results of the FSF experiments with and without an integrating action. Table 8 summarizes some important metrics from these experiments, such as position error, RMS, and overshoot. Figure 27 compares the FSF with integrating action to the PID-PI-FF controller were the poles are placed at the location as explained in 4.2.3 are used, and Table 9 presents the derived metrics. Additional experiments were conducted with the FSF controller with integrating action on a reference trajectory, with and without pressure references, as depicted in Figure 28 and Figure 29.

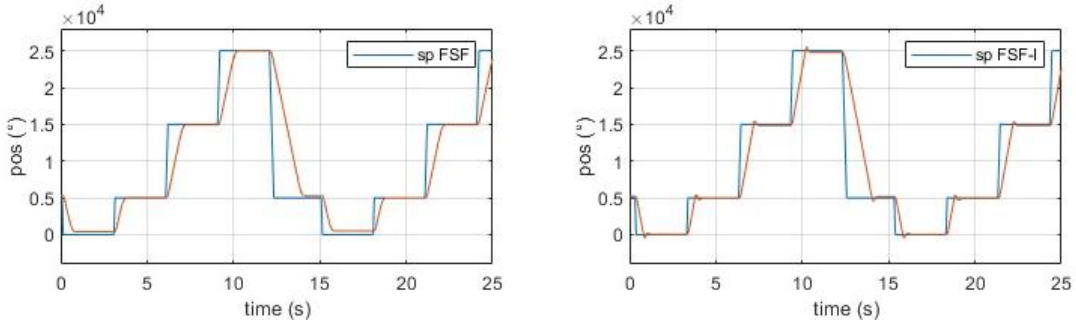

Figure 26 point-to-point control for FSF without I action (left) and with I action (right). With 4th Butterworth poles.

Table 8 Comparison FSF with and without integrator with 4th Butterworth poles.

	FSF with I action	FSF
Position error and RMS (°)	35.7 ± 154 °	-167 ± 222 °
% overshoot	5.6%	0.4%
Settling time avg (s); % settling within 5(s)	2.5 (s); 100%	1.3 (s); 100%
Rise time avg (s)	0.57 (s)	0.49 (s)
Hunting Bandwidth (°)	0	0

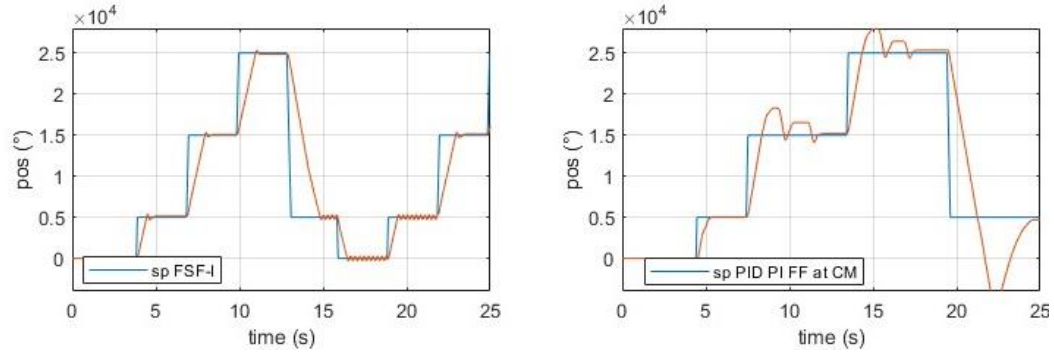

Figure 27 point-to-point control with comparable pole placement PID-PI-FF(right) and FSF with I action(left).

Table 9 metrics for comparable pole placement FSF with I action and PID-PI-FF control.

	FSF with I action	PID-PI-FF at CM
Position error and RMS (°)	97.26 ± 212 °	-43.3 ± 215 °
% overshoot	4.7%	54.5%
Settling time avg (s); % settling within 5(s)	2.5 (s); 81%	3 (s); 73%
Rise time avg (s)	0.57 (s)	1.24 (s)
Hunting Bandwidth (°)	300 °	0

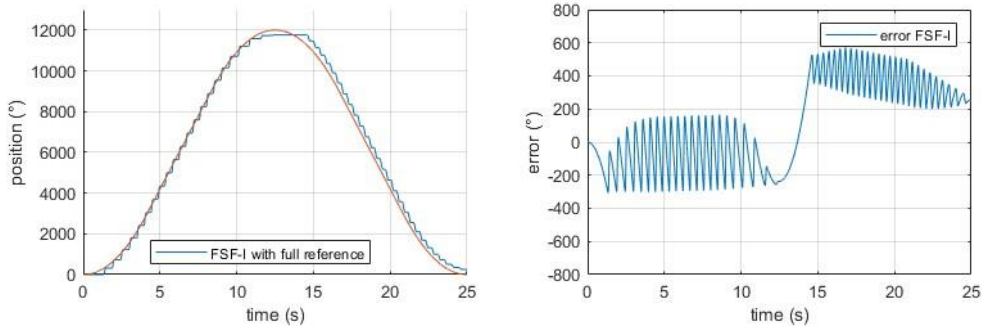

Figure 28 Trajectory control of FSF-I with full pressure reference and poles placed at 4th Butterworth poles location.

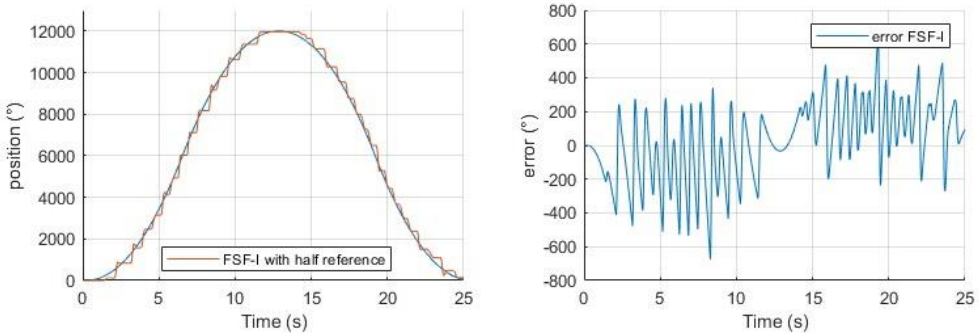

Figure 29 Trajectory control of FSF-I without pressure reference and poles placed at 4th order Butterworth poles location.

Figure 30 depicts the trajectory performance of the FSF with a integrator controller and the PID-PI-FF controller the reference trajectory consist of only the position and velocity for better comparability. Lastly, both closed loop system have their poles placed as described in section 4.2.3.

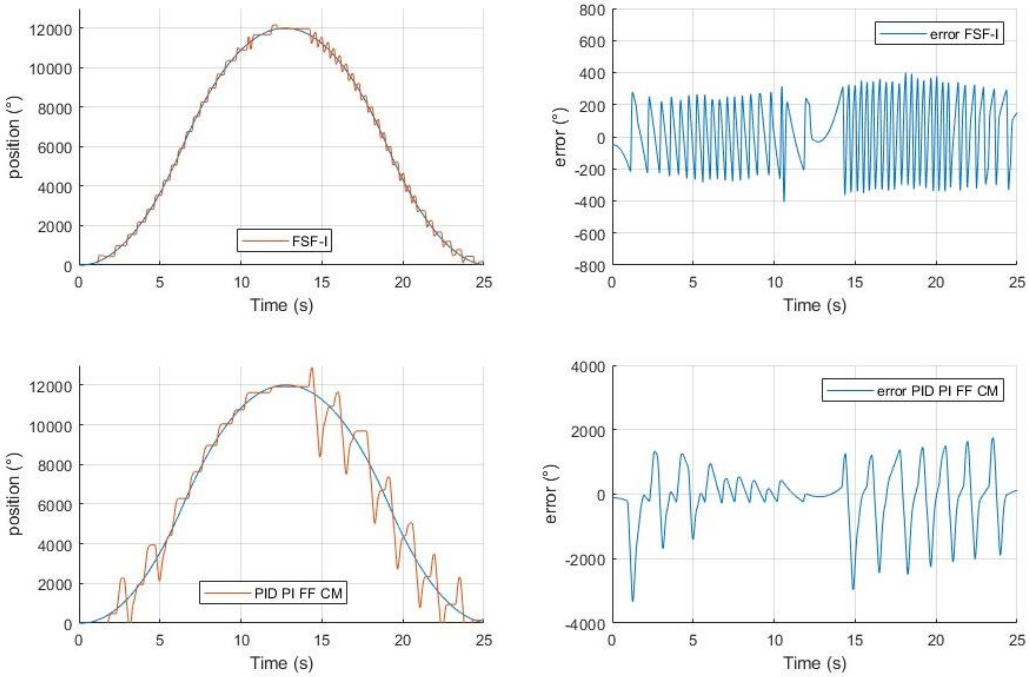

Figure 30 Trajectory control FSF-I and PID-PI-FF measured at the CM with comparable pole placement.

4.4. Discussion

Figure 26 depicts the setpoint control of the full-state feedback controller. It is clear that the control without an integrating action has no overshoot and a large steady-state error. The addition of an integrator significantly reduces the steady state error, but with some overshoot which is probably caused by integrator windup. When, both PID-PI-FF and the FSF-I controllers are compared with comparable pole locations one would expect similar system behavior. This, however is not observed, as depicted in Figure 27. One possible explanation could be that the slightly dampened conjugate pole pair at -36 of the PID-PI-FF controller, as depicted in Figure 25 is dominant.

The full state feedback controller uses the dynamical model as described in section 2.7 to place the poles at the desired locations. However, the parameters of this dynamical model where obtained through an FRF at a nominal 0.5 MPa inlet pressure. It is possible that the model is not valid for higher non-nominal system inlet pressures. When this nonlinear system is linearized and used for tuning of the PID-PI-FF controller, neither great trajectory or setpoint control is observed, as seen in chapter 4.3. Additionally, the choice to use a linearized model instead of a transfer function directly fitted to the FRF resulted in slight misfit between the model and system. As a result, the choice to use the PID-PI-FF closed loop poles for comparison with full state feedback controller is questionable. Furthermore, no effort was made to verify the poles and zeros of the closed loop plant with the PID-PI-FF controller via a FRF.

Figure 29, and Figure 28 show the results of the trajectory tracking. When, a pressure reference is used, better tracking performance is achieved. Also, the effect of the integrating action works but is not perfect, as seen in Figure 28. Where, in the descending trajectory the error is initially rather large and is minimized over time. Lastly, the trajectories of the FSF-I shows better tracking performance when compared to the PID-PI-FF controller for both manual and comparable pole placement .

Therefore, it can be concluded that FSF-I controller shows superior point-to-point and tracking performance when compared to the previously designed PID-PI-FF controller in terms of overshoot, settling time, and rise time. Also, the addition of a full reference trajectory reduces the error slightly. Additionally, the implemented FSF controller gives great control over the desired system behavior. Where the manual pole placement with 4_{th} order Butterworth poles showed the best point-to-point performance for the FSF controller. However, the problem of time delay or the non-linearities are not yet accounted for.

5. Feedback linearization

This chapter first motivates the use of output feedback linearization. Then, the theory behind input to output linearization is explained. Next, the implementation and its difficulties are mentioned. Lastly, the results are showed and discussed.

5.1. Motivation

The results from the FSF controller showed better performance for both setpoint and trajectory control in comparison with the PID-PI-FF controller. However, the FSF controller still uses a linearized state space representation of the nonlinear dynamic model. Unfortunately, this model is not valid for pressures deviating from the states used for linearization. Therefore, implementing a nonlinear control technique such as input to output feedback linearization (IOFL), could improve the point-to-point and trajectory performance. The nonlinear controller is expected to improve setpoint and tracking performance by transforming the input to output relationship of the nonlinear system into a linear one.

5.2. Theory

IOFL is a control technique used for nonlinear control systems. Where, the aim is to obtain a linear relationship between the input and output, such that the transformed system only has linear terms left, which allows the use of standard linear control techniques. A generic block diagram for IOFL is given in Figure 31, this chapter describes each of mentioned blocks in this diagram for a SISO system. Furthermore, the requirements for a system to be feedback linearizable are described in Appendix B: Feedback linearizable systems .

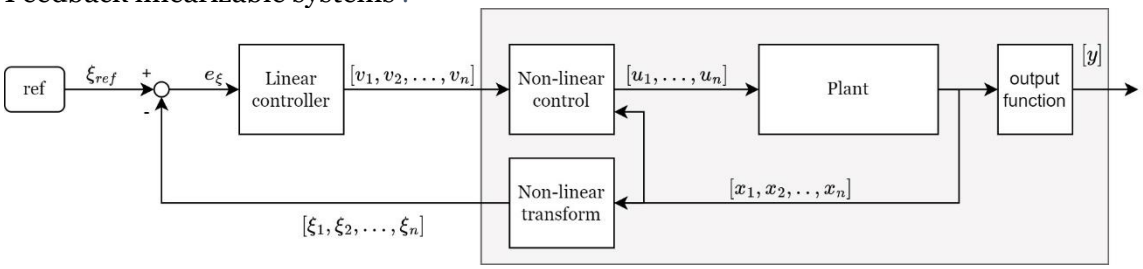

Figure 31 Block diagram for IOFL controller

First, a class of nonlinear systems is considered, as mentioned in [20]

$$\dot{x} = f(x) + g_i(x)u \qquad 5.1$$
$$y = h(x),$$

where $h(x)$ and $f(x)$ are vectors of dimension n of nonlinear functions, and $g_i(x)$ is an $(n\ x\ m)$-matrix of nonlinear functions. This chapter describes the generic SISO case where $m = 1$ and n is the order of the system.

The chosen control law is

$$u = \beta(x)^{-1}(-\alpha(x) + v), \qquad 5.2$$

Where $\beta(x)$ is the decoupling scalar and $\alpha(x)$ the dynamic scalar, v is the linear control scalar. The input to output relationship can be obtained through differentiating the vector functions $h(x)$ from equation *5.1* until at least one input appears. This number of differentiations, named relative degree ρ satisfies $1 \leq \rho \leq n$. Where n is the order of the system.

The time derivate of a output for a SISO system described using Lie derivatives is given by

$$y^{(\rho)} = L_f^{\rho} h(x) + \sum_{i=1}^{p} L_{g_i} L_f^{\rho-1} h(x) u_i \quad i = p, \tag{5.3}$$

where $y^{(\rho)}$ are the ρ order time derivatives of output y and p is the amount of inputs of the system. $L_f^{\rho} h(x), L_{g_i} L_f^{\rho-1} h(x)$ are the Lie derivatives of the output equation $h(x)$ with respect to the state function $f(x)$ and the input function $g_i(x)$ [20]. The Lie derivatives until the second order are given below

$$L_f h(x) = \frac{\partial h(x)}{\partial x} f(x), \qquad L_{g_i} h(x) = \frac{\partial h(x)}{\partial x} g_i(x)$$
$$L_f^2 h(x) = \frac{\partial L_f h(x)}{\partial x} f(x), \qquad L_{g_i} L_f h(x) = \frac{\partial L_f h(x)}{\partial x} g_i(x). \tag{5.4}$$

The nonlinear system as in equation *5.1* is said to have relative degree ρ if

$$L_{gi} L_f^n h(x) = 0, 0 < n < \rho - 1$$
$$L_{gi} L_f^n h(x) \neq 0, n = \rho - 1. \tag{5.5}$$

5.2.1. Non-linear transformation

This chapter explains how the system states are transformed into the new normal coordinate state vector ξ. When IOFL is performed the system dynamics are split into an internal and external part [20]. Where, the external part are the system states who are controllable from the system inputs. This is the case when $\rho = n$, in this case no internal dynamics exist and the non-linear transformation is defined as

$$z = \begin{bmatrix} y \\ \vdots \\ \vdots \\ y^{\rho-1} \end{bmatrix} = \begin{bmatrix} h(x) \\ L_f h(x) \\ \vdots \\ L_f^{n-1} h(x) \end{bmatrix} = [\xi]. \tag{5.6}$$

5.2.2. Closing the loop

The relationship between the ρ order time derivatives from equation *5.3* and the chosen control law from equation *5.2* one can define the $\beta(x)$, and $\alpha(x)$ scalars as

$$\beta(x) = L_{g1} L_f^{\rho-1} h(x), \alpha(x) = L_f^{\rho} h(x). \tag{5.7}$$

Because, the control law uses the inverse of $\beta(x)$ which is a scalar and is thus always reversible. Next, the linear control scalar v is obtained though applying full state feedback control

$$v = -K(\xi_{ref} - \xi), \tag{5.8}$$

where a new state vector ξ in the normal form is required which is defined as

$$\xi = \left[y, y^{(2)}, \dots, y^{(\rho+1)}\right]. \tag{5.9}$$

The theory behind full state feedback is explained in chapter 4. Additionally, equation *5.8* requires a reference signal ξ_{ref} which is explained in section 5.3.

The ability to use feedback to convert a nonlinear state equation into a linear one by cancelling nonlinearities requires the nonlinear state equation to have the following structure[20].

$$\dot{\xi} = A_c\xi + \mathrm{B}_c\beta(x)\left[u - \frac{\alpha(x)}{\beta(x)}\right], \qquad 5.10$$
$$y = C_c\xi.$$

where $\beta(x)$ and $\alpha(x)$ are the decoupling an dynamic scalars, and A_c, B_c, and C_c are the state space matrices in normal form

$$A_c = \begin{bmatrix} 0 & 1 & 0 & \cdots & 0 \\ 0 & 0 & 1 & \cdots & 0 \\ \vdots & \vdots & \vdots & \cdots & \vdots \\ 0 & 0 & 0 & \cdots & 1 \\ 0 & 0 & 0 & \cdots & 0 \end{bmatrix}_{\rho\times\rho}, B_c = \begin{bmatrix} 0 \\ 0 \\ \vdots \\ 1 \end{bmatrix}_{1\times\rho}, C_c = [1\ 0\ 0\ \cdots 0]_{\rho\times 1}, \qquad 5.11$$

with ρ being the relative degree of the plant. After substitution of the chosen control law from equation *5.2* in equation *5.10* the system reduces to

$$\dot{\xi} = A_c\xi + \mathrm{B}_c v. \qquad 5.12$$

This form shows the decoupled behavior and is similar to the basic equation used to design the full state feedback controller as seen in chapter 4.

5.3. Implementation

This section describes the steps taken with the explained principles from chapter 5.2 and the difficulties faced when implementing the IOFL control. The 4th order nonlinear system as described in equation 2.11 is used, where the state vector is described as $x = [\theta\ \omega\ P_{lin}\ P_{lout}]^T$. The implemented block scheme is depicted in Figure 32. The first step involves the selection of a output vector, in this case only the position output is relevant and the output is therefore chosen as $y = \theta$.

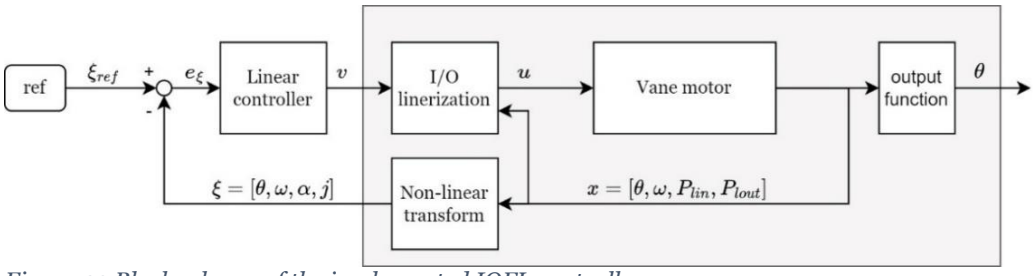

Figure 32 Block scheme of the implemented IOFL controller

The next step involves obtaining the relative degree, where the output is four times differentiated until the input appeared. Which resulted in a case were $\rho = n$, in this case no zero dynamics are present. The output and the higher order time derivatives are

$$y = h_1(x) = \theta, \qquad 5.13$$
$$y^2 = \dot{y_1} = L_f h_1(x) = \omega,$$
$$y^3 = \ddot{y_1} = L_f^2 h_1(x) = \frac{\left(x_3 - sgn(x_2)\left(f_{stat} - f_{dyn1}x_2 - f_{dyn2}x_2^2\right)\right)D_{ia}}{I} = \alpha,$$
$$y^4 = \dddot{y}_1 = L_f^3 h_1(x) = j,$$
$$y^5 = L_f^4 h_1(x) + L_{g1}L_f^3 h_1(x)u_1,$$

where the $sgn(x_2)$ function is implemented as

$$sgn(x_2) = \begin{cases} -1 \; if \; x_2 < 0 \\ 0 \; if \; x_2 = 0 \\ 1 \; if \; x > 0 \end{cases}. \quad 5.14$$

The Lie derivatives are calculated with the symbolic toolbox in MATLAB and the difflie() function from [21]. The resulting transformed coordinates are

$$\xi = [\theta, \omega, \alpha, j], \quad 5.15$$

with $\theta, \omega, \alpha, j$ are the position, angular velocity, acceleration, and jerk. All of the Lie derivatives are given in: Appendix C: Lie derivatives.

The selected control law from equation 5.2 with the decoupling scalar $\beta(x)$, and the dynamic scalar $\alpha(x)$ is defined as

$$u = \frac{1}{L_{g1}L_f^3 h_1(x)}(-L_f^4 h_1(x) + v). \quad 5.16$$

The obtained control law is first implemented in Simulink and showed singular behavior for $\omega = 0$. Setting the initial condition for the proportional valve as fully opened solved this problem. Furthermore, the transformation of the state vector ξ is calculated through taking the time derivative of the position several times. The method for the angular velocity is $\omega = \Delta\theta/\Delta t$ where Δt is the sampling time of 1 ms. An identical approach is also used for the higher order time derivatives. Theoretically, these higher order time derivatives are calculated with the obtained formulas. However, taking the derivatives of the position eliminates possible model errors.
In TWINCAT3, the reference signal ξ_{ref} is created with a 3 phase setpoint generator that generates the reference position, velocity, acceleration, and jerk [16]. Where for setpoint control a reference signal with a maximum velocity near the actual vane motor max velocity is chosen. The set parameters are mentioned in Table 10.

Table 10 Reference signal setpoint control

Velocity Max ($°/s$)	Acceleration ($°/s^2$)	Jerk Max ($°/s^3$)
$1.5 * 10^3$	$1 * 10^3$	$7.5 * 10^5$

The last step involved obtaining the gain matrix K in the chosen linear control law from equation *5.8*.

5.3.1. Pole placement

The closed loop system response of the vane motor with the IOFL controller are matched to the earlier implemented PID-PI-FF and FSF controller for comparability. This should be achieved with choosing identical poles as depicted in Figure 25. Placing the IOFL controller poles was done with the place() command in MATLAB. Where the new normal form state space matrices are

$$A_c = \begin{bmatrix} 0 & 1 & 0 & 0 \\ 0 & 0 & 1 & 0 \\ 0 & 0 & 0 & 1 \\ 0 & 0 & 0 & 0 \end{bmatrix}, B_c = \begin{bmatrix} 0 \\ 0 \\ 0 \\ 1 \end{bmatrix}, C_c = [1\ 0\ 0\ 0]. \quad 5.17$$

This pole placement method calculates the gain vector K for the state feedback control law $v = -K(\xi - \xi_{ref})$ with the following equation

$$\det|sI - (A_c - B_c K)| = 0. \quad 5.18$$

5.4. Results

Figure 33 depicts the setpoint control of the IOFL controller. The chosen setpoint was a pseudo random number between 0 and 25000°. The measured data was translated into different metrics, as shown in Table 10. Since the settling time and rise time are dependent on the chosen trajectories, they are not mentioned in the table. Additionally, Figure 34 depicts the output of the controller, where it can be observed that all of the outputs show a fully opened or closed valve. Lastly, Figure 35 depicts the trajectory control of the IOFL controller.

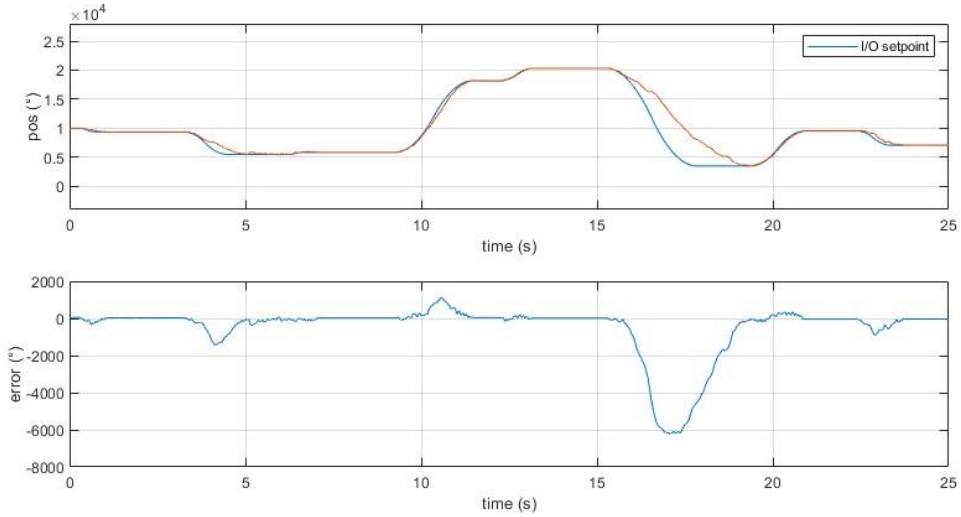

Figure 33 Setpoint control for IOFL controller

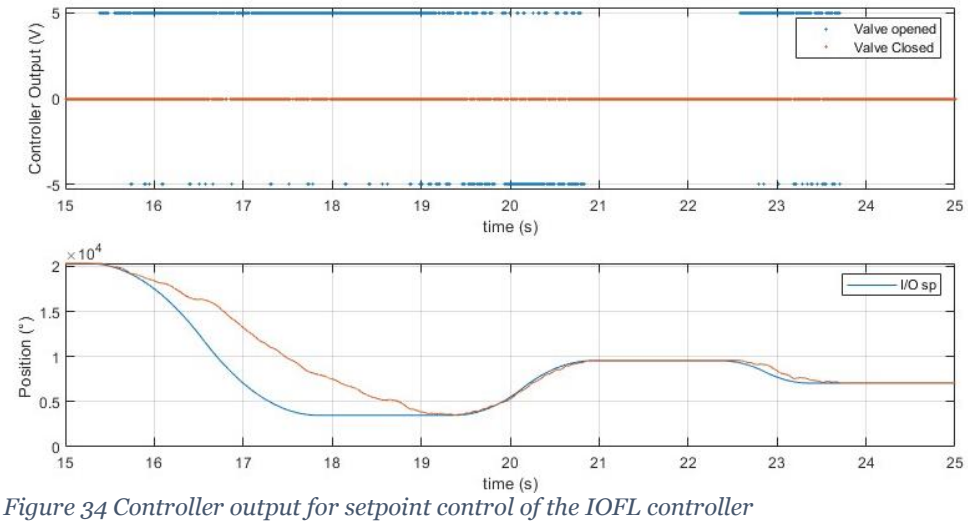

Figure 34 Controller output for setpoint control of the IOFL controller

Table 11 derived metrics for the IOFL controller

	IOFL controller
Position error and RMS (°)	18±41.8°
% overshoot	3.6%
Settling time avg (s) ; % settling within 5(s)	–; 100%
Rise time avg (s)	–
Hunting Bandwidth (°)	0

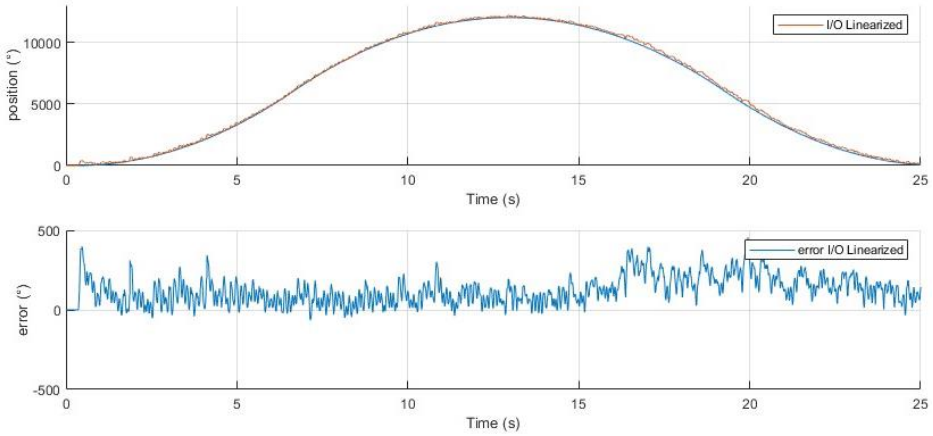

Figure 35 Trajectory control of the IOFL controller

5.5. Discussion

Table 11 shows that the IOFL controller is capable of decent setpoint accuracy and repeatability. Unfortunately, the tracking behavior for the downward trajectories in Figure 33 shows unwanted behavior. Analyzing the controller output as depicted in Figure 34 shows a few interesting points. Firstly, the proportional valve is only fully opened or closed, thus making this component obsolete. Also, in some instances, the control output sign flipped where this was not required. This may be caused by the transformation coordinates being the higher order time derivatives of the position which results in a really noisy signal. The above point plus the knowledge of the direction-dependent friction and really low inertia of the VM could explain why the systems is following the trajectory poorly. A solution might be to use the Lie derivatives instead of the higher order time derivatives or to reduce the reference acceleration and jerk.

Figure 35 shows the trajectory control of the IOFL controller. The trajectory to be followed has an acceleration of only 300 $°/s^2$, leading to a significant reduction of the position error when compared to setpoint control trajectory as depicted in Figure 33. However, the error primarily remains positive, likely due to side-dependent friction which results in the VM accelerating quicker in the positive direction. The addition of a integrating action would probably solve this offset.

The IOFL controller is expected to enhance setpoint and trajectory accuracy compared to the FSF-I controller. Indeed, some improvement is observed in both setpoint and trajectory control. However, IOFL assumes perfect cancellation of the nonlinear terms to achieve a linear system. In reality, this cancellation is probably not perfect because of uncertainties like noise. Due to this, the system behavior for some uncertainties in the parameters should still be evaluated to check robustness.

6. Removing the proportional valve

In this chapter, additional results are presented using the FSF, IOFL, and PID-PI-FF controller without the proportional valve. The purpose of these experiments is to demonstrate that the proportional valve is not necessary and to enable a better comparison with the already implemented SMC and PD-PWM controller who also do not utilize the proportional valve. In chapter 6.2, the results obtained from these experiments are discussed in detail.

6.1. Results

Figure 36 compares the setpoint control of the FSF-I, PID-PI-FF, and the IOFL controller. The FSF-I reference consist only of the position. Further details are presented in Table 12.

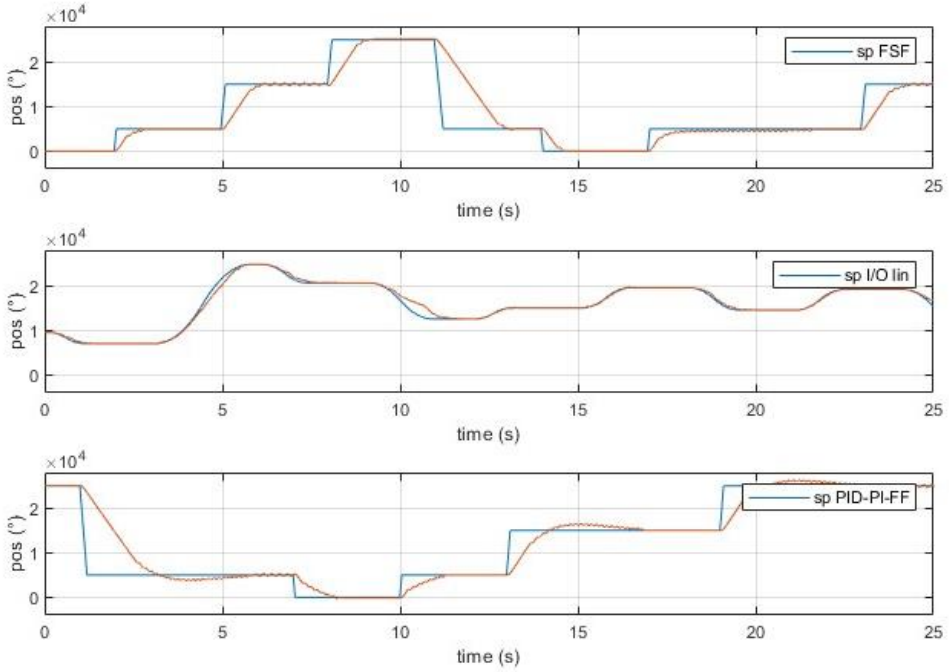

Figure 36 setpoint control of FSF-I,PID-PI-FF ,and IOFL controller without the proportional valve

Table 12 Comparison between FSF-I, PID-PI-FF, and IOFL controller with - and without the proportional valve

	FSF with I action	IOFL	PID-PI-FF CM
	With proportional valve		
Position error and RMS (°)	35.7 ± 154 °	18±41.8°	95 ± 173.6°
% overshoot	5.6%	3.6%	22.5%
Settling time avg (s); % settling within 5(s)	2.5 (*s*); 100%	–; 100%	2.3(*s*); 70%
Rise time avg (s)	0.57 (*s*)	–	0.64(*s*)
Hunting Bandwidth (°)	0	0	0
	Without proportional valve		
Position error and RMS (°)	47.76 ± 187 °	4.77 ± 38.9°	−32.06 ± 99 °
% overshoot	2.4%	2.57%	7.3%
Settling time avg (s); % settling within 5(s)	2.5 (*s*); 60%	–; 100%	3.86 (*s*); 63%
Rise time avg (s)	0.57 (*s*)	–	0.75(*s*)
Hunting Bandwidth (°)	310 °	0	300 °

6.2. Discussion

The results of the IOFL controller chapter 5.4 shows that the proportional valve could not keep up with the controller output. After removing this component, new results are obtained, as depicted in Figure 36. Firstly, the downward trajectories of the IOFL controller shows a little improvement over the case where the proportional valve is used. Also, all of the metrics of the IOFL controller are improved, as shown in Table 12 . This confirms our belief that the proportional valve is indeed bottlenecking the system.

Lastly, for PID-PI-FF significant improvement of the position accuracy and repeatability is seen. Unfortunately, hunting movement is more often observed, which reduces the "% settling within 5 seconds" metric. This is probably solved though enlarging the error bandwidth between which both fast switching valves should be closed.

7. Conclusion

This work focused on the question if improvements can be made on the point to point and trajectory control for a MR/CT safe vane motor. Three different controllers were implemented and tested. First, a cascade PID-PI controller with feedforward was implemented to control the pressure first and with the pressure a position. The feedforward term was integrated to cope with disturbances such as dynamic friction. Secondly, a full state feedback controller was implemented and tested to have more control over the system response. Also, an additional integrator action was introduced to reduce steady state error. Lastly, a input to output feedback linearization controller was designed to cope with the nonlinear dynamics of the vane motor. All of the results where then compared to the already implemented PD-PWM and SMC controllers.

Initial results of the PID-PI-FF showed that both setpoint and trajectory control performance where both significantly worse than the already implemented SMC and PD-PWM controller. Also, not all requirements as mentioned in chapter 2.1 where satisfied. For example: the setpoint control settling time was often above the 5 seconds threshold. Remarkably, it can be concluded that the pressure measurement via a tube feeding back to the control module will reduce overshoot and improve accuracy and repeatability slightly. Unfortunately, the addition of feedforward did not improve point-to-point control and trajectory control performance.

The best obtained point-to-point control for FSF was achieved with the FSF-I controller with an accuracy and repeatability of 35.7±154°, which is almost similar to the PD-PWM controller. However, the nonlinear SMC still achieved superior point-to-point and trajectory control performance. The peak error for trajectory control with a position and velocity reference was 600°, where the addition of a pressure reference improved the maximum error to 550°. This full reference made the FSF-I controller performance similar to the PD-PWM controller and SMC but only in the positive upwards direction. An important remark is that the implemented FSF controller gave great control over the desired system behavior, making tuning a lot easier when compared to the PID-PI-FF controller.

The designed input-to-output feedback linearizable controller achieved good results for both point-to-point and trajectory control. With a accuracy and repeatability of 18±41.8° for point-to-point control, which is similar to SMC and better than the PD-PWM controller. Furthermore, this controller was capable of keeping the trajectory error variance mostly between 250°, which is superior to the SMC and similar to the PD-PWM. Also, the error on the upwards positive trajectory is a bit smaller when compared to the SMC and PD-PWM. However, tuning the IOFL controller to obtain the desired system behavior was hard. In most cases, only a really aggressive high-frequent controller output was seen, where the VM proportional valve could not keep up. The research showed that the removal of this proportional valve at 0.5 MPa inlet pressure did indeed improve setpoint accuracy and repeatability for the IOFL controller, up to 4.77±38.9°, which is significantly better than the SMC and PD-PWM controller.

Lastly, this research showed that in general aggressive control which fully opens or closes the valves instead of controlling the mass flow or pressure is performing better for both trajectory and point-to-point control.

8. Recommendations

The implementation of an observer to estimate the inlet vane motor pressure instead of measuring would reduce the added time delay and the extra pressure drop which is added through the feedback lines to the CM. The vane motor position accuracy shows some variance due unknown disturbances. The addition of a disturbance observer for both full state feedback and the IOFL controller could improve point-to-point and trajectory control.

Additionally, the vane motor suffers from direction-dependent friction. Therefore, implementing different friction models per rotation direction would be beneficial.

Furthermore, additional research is required for the IOFL controller. Several improvements can be made, including the use of a tame differentiators or the derived Lie derivatives for the state transformation to smoothen the system response. Also, the addition of a integrating action would decrease the average position error.

Lastly, The vane motor has an anti-backlash mechanism, as explained in section 1.1. This mechanism is designed to solve the issue of uncertainty due to backlash and should be used to test if more accurate point-to-point needle positioning is possible.

9. References

[1] M. Menno Arnolli, “from scratch to clinic-Development of a precision system for image-guided needle placement,” PhD, University Twente, Enschede. doi: 10.3990/1.978903654332-3.

[2] J. Mulder, “Design and Development of an MR Safe Servomotor,” EngD, University Twente, Enschede, 2019.

[3] A.Vogelzang, “Understanding the new MR-safe drive system of the NPS.,” Msc , University Twente, Enschede, 2022.

[4] Y. Zhang and A. Nishi, “Low-pressure air motor for wall-climbing robot actuation,” *Mechatronics*, vol. 13, no. 4, pp. 377–392, May 2003, doi: 10.1016/S0957-4158(01)00047-2.

[5] S. Y. Chen, Y. H. Hung, and S. S. Gong, “Speed Control of Vane-Type Air Motor Servo System Using Proportional-Integral-Derivative-Based Fuzzy Neural Network,” *International Journal of Fuzzy Systems*, vol. 18, no. 6, pp. 1065–1079, Dec. 2016, doi: 10.1007/S40815-015-0134-0/TABLES/1.

[6] S. Ning and G. M. Bone, “Experimental comparison of two pneumatic servo position control algorithms,” *IEEE International Conference on Mechatronics and Automation, ICMA 2005*, pp. 37–42, 2005, doi: 10.1109/ICMA.2005.1626519.

[7] D. Meng, B. Lu, A. Li, J. Yin, and Q. Li, “Pressure Observer Based Adaptive Dynamic Surface Control of Pneumatic Actuator with Long Transmission Lines,” *Appl. Sci. 2019, 9(17)*, 2019, doi: 10.3390/app9173621.

[8] C. H. Lu and Y. R. Hwang, “Modeling of an air motor servo system and robust sliding mode controller design,” *Journal of Mechanical Science and Technology*, vol. 26, no. 4, pp. 1161–1169, Apr. 2012, doi: 10.1007/S12206-012-0220-2/METRICS.

[9] M. Turkseven and J. Ueda, “Model-Based Force Control of Pneumatic Actuators with Long Transmission Lines,” *IEEE/ASME Transactions on Mechatronics*, vol. 23, no. 3, pp. 1292–1302, Jun. 2018, doi: 10.1109/TMECH.2018.2832986.

[10] Krasnow.B, “Fiberoptic joystick with quadrature encoders and arduino.” Accessed: Nov. 20, 2023. [Online]. Available: https://benkrasnow.blogspot.com/2010/12/fiberoptic-joystick-with-quadrature.html

[11] markos rodrigo, “Fluid Mechanics seventh edition by Frank M. White.” Accessed: Jan. 06, 2024. [Online]. Available: https://www.academia.edu/31884719/Fluid_Mechanics_seventh_edition_by_Frank_M_White

[12] “Series LRWA analogic proportional servo valves Analogic proportional servo valves Flow control-Series LRWA”, Accessed: Jan. 06, 2024. [Online]. Available: www.camozzi.com.

[13] “de juiste ademhaling.” Accessed: Nov. 20, 2023. [Online]. Available: https://hantayo.nl/artikelen/juiste-ademhaling

[14] H. K. Lee, G. S. Choi, and G. H. Choi, “A study on tracking position control of pneumatic actuators,” *Mechatronics*, vol. 12, no. 6, pp. 813–831, Jul. 2002, doi: 10.1016/S0957-4158(01)00024-1.

[15] “Designing Cascade Control System with PI Controllers - MATLAB & Simulink - MathWorks Benelux.” Accessed: Nov. 29, 2023. [Online]. Available:

https://nl.mathworks.com/help/control/ug/designing-cascade-control-system-with-pi-controllers.html#Introduction%20to%20Cascade%20Control
[16] Beckhoff, "TF4100 | TwinCAT 3 Controller Toolbox."
[17] R.G.K.M. Aarts, G.R.B. Romer, Dr. H. Koro, J. van Dijk, and C. van Keulen, *DESIGN & CONTROL OF MECHATRONIC SYSTEMS*. 2021.
[18] "PID Tuning Guide." Accessed: Jan. 08, 2024. [Online]. Available: https://tlk-energy.de/blog-en/practical-pid-tuning-guide
[19] "Full state feedback - Wikipedia." Accessed: Nov. 17, 2023. [Online]. Available: https://en.wikipedia.org/wiki/Full_state_feedback
[20] hassan-khalil, *nonlinear-systems*. Prentice Hall, 2002.
[21] "difflie(X, Y, variables) - File Exchange - MATLAB Central." Accessed: Nov. 30, 2023. [Online]. Available: https://nl.mathworks.com/matlabcentral/fileexchange/65287-difflie-x-y-variables
[22] W. Ohnishi, H. Fujimoto, K. Sakata, A. Hara, and K. Saiki, "Trajectory tracking control for pneumatic actuated scan stage with time delay compensation," *IECON Proceedings (Industrial Electronics Conference)*, pp. 5125–5130, Dec. 2016, doi: 10.1109/IECON.2016.7793764.
[23] M. I. P. Azahar and A. Irawan, "Enhancing Precision on Pneumatic Actuator Positioning using Cascaded Finite-time Prescribed Performance Control," *Proceedings - 2021 11th IEEE International Conference on Control System, Computing and Engineering, ICCSCE 2021*, pp. 131–136, Aug. 2021, doi: 10.1109/ICCSCE52189.2021.9530956.
[24] J. Mohorcic and L. Dong, "Extended state observer-based pressure control for pneumatic actuator servo systems," *Control Theory and Technology*, vol. 19, no. 1, pp. 64–79, Feb. 2021, doi: 10.1007/S11768-021-00038-Y/FIGURES/16.
[25] W. Wang and D. Meng, "Output feedback motion control of pneumatic servo systems with desired compensation approach," *Journal of the Brazilian Society of Mechanical Sciences and Engineering*, vol. 42, no. 6, pp. 1–12, Jun. 2020, doi: 10.1007/S40430-020-02370-X/FIGURES/13.
[26] M. Smaoui, X. Brun, D. Thomasset, M. Smaoui, X. Brun, and D. Thomasset, "A study on tracking position control of an electropneumatic system using backstepping design A study on tracking position control of an elec-tropneumatic system using backstepping design A study on tracking position control of an electropneumatic system using backstepping design," *Control Eng Pract*, vol. 14, no. 8, 2006, doi: 10.1016/j.conengprac.2005.05.003ï.
[27] A. min Li, D. yuan Meng, B. Lu, and Q. yang Li, "Nonlinear cascade control of single-rod pneumatic actuator based on an extended disturbance observer," *J Cent South Univ*, vol. 26, no. 6, pp. 1637–1648, Jun. 2019, doi: 10.1007/S11771-019-4118-3/METRICS.
[28] M. Choux, G. Hovland, and M. Blanke, "Cascade Controller Including Backstepping for Hydraulic-Mechanical Systems," *IFAC Proceedings Volumes*, vol. 45, no. 8, pp. 310–315, Jan. 2012, doi: 10.3182/20120531-2-NO-4020.00046.
[29] M. Choux and G. Hovland, "Adaptive backstepping control of nonlinear hydraulic-mechanical system including valve dynamics," *Modeling, Identification and Control*, vol. 31, no. 1, pp. 35–44, 2010, doi: 10.4173/MIC.2010.1.3.

10. Appendices

10.1. Appendix A: Overview Literature study

Linear control

Linear control techniques, such as PI (Proportional-Integral) and PID (Proportional-Integral-Derivative) controllers, have found wide application in the control of pneumatic actuator systems. The control schemes in found papers are illustrated in Figure 4.

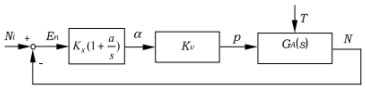

(d) Zhang et al.
Illustration from [4]

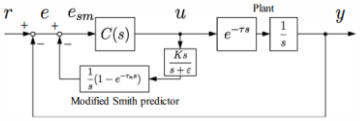

(e) Wataru et al.
Illustration from [22]

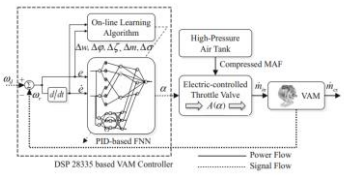

(f) Yi chen et al.
Illustration from [5]

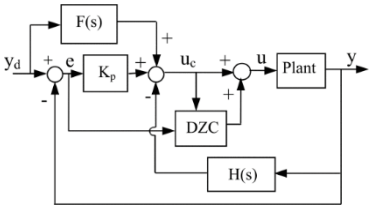

(g) Ning et al.
Illustration from [6]

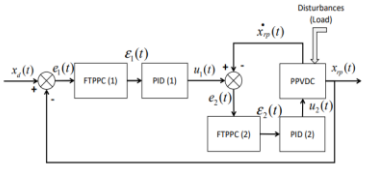

(h) Iskandar putra et al.
Illustration from [23]

Figure 37 Linear control schemes

In the field of rotary-type air motors, early implementations of PI controllers were explored by Zhang et al [4] . This particular study employed a model-based approach using a PI controller to regulate position and velocity. However, this study did not consider delays, uncertainties, or disturbances.

In more recent research, a cascade PI controller with a modified Smith predictor was proposed to address time delay in the hoses of a cylinder-type air motor [22]. The results showed improved position tracking performance, when compared to only PI control.

Yi chen et al. [5], proposes a model free approach were a fuzzy neural network (FNN) is used to tune PID control parameters for a vane-type motor. An improvement in speed tracking was seen when compared to normal PID, also the proposed FNN-PID controller was more robust.

Another technique, proposed by Iskandar putra et al.[23] utilize a finite time prescribed performance control with cascade PID (FTPPC-CPID) for a cylinder type actuator. When compared to cascade PID great improvement was seen over a wide range of trajectories, an advantage of this method is that complex parameter regulation is avoided completely.

Lastly, a study from Ning et al. [6] presented a controller known as Position plus Velocity plus Acceleration feedback combined with Feedforward and Deadzone Compensation

(PVA+FF+DZC). It was compared with a nonlinear sliding mode controller, and the results demonstrated the superiority of the sliding mode controller over the PVA+FF+DZC method.

Non-linear control

Nonlinear control techniques are better suited for controlling the vane-motor due to its strong nonlinear dynamics. However, these techniques have increased complexity. Examples of nonlinear control techniques include feedback linearization, backstepping, and sliding mode control(SMC).

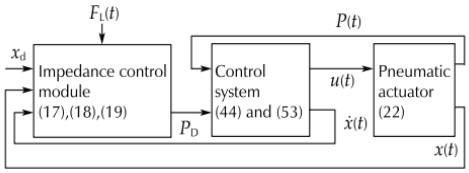

(c) Mohorcic et al. Adapted from [24]

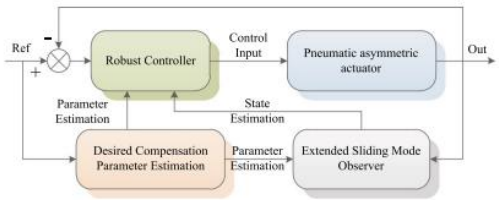

(d) Wang et al. Adapted from [25]

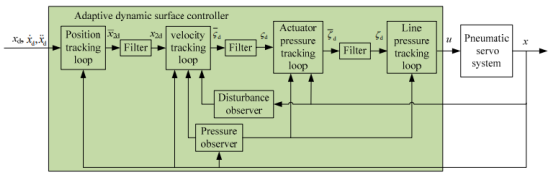

(e) Meng et al. Adapted from [7]

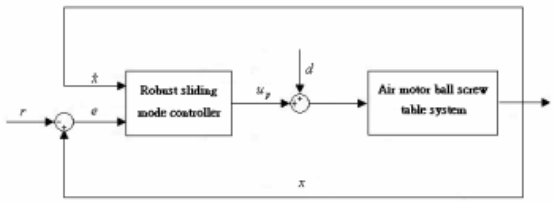

(f) Lu et al. Adapted from [8]

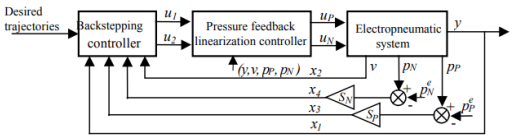

(g) Smaoui et Al. Adapted from [26]

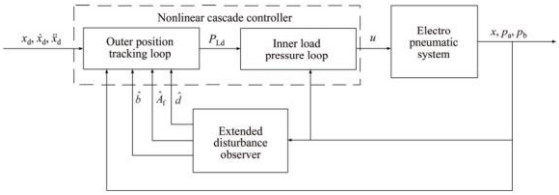

(h) Ai-min et Al. Adapted from [27]

Figure 38 Nonlinear control schemes

To overcome the effect of uncertainties such as leakage and friction Lu et al. [8] proposes a robust SMC design. The research results demonstrate that sliding mode control effectively handles the nonlinearities which come from air compressibility and friction.

In another paper from Mohorcic et al. [24], an extended state observer-based sliding mode controller is proposed. This controllers consist of a impedance control module and a control system. The control module takes payload force, position and velocity into account and outputs the desired pressure. The control system uses SMC and ESO to compensate for the disturbances. The findings indicate that active disturbance rejection control ADRC and ESO-based SMC outperform SMC in terms of tracking performance.

Another study from Wang et al. [25] proposes an extended sliding mode observer (ESMO) together with a robust controller. The controller uses a desired compensation parameter-adaptive method that utilizes the desired system state instead of measured states. The results indicate that the proposed controller outperforms a PID controller. However, it should be noted that there is no systematic approach provided for tuning the controller parameters.

Ai-min et Al. [27] propose a different approach to address the nonlinearities and disturbances in a pneumatic cylinder-type actuator. The introduced control scheme uses an extended state disturbance observer with a nonlinear cascade controller, which is developed using the backstepping method. The results demonstrate that the implemented controller does not outperform an adaptive robust controller.

One notable source that explored the topic of an MRI-safe controller with long transmission lines is a publication by Meng et al. [7], which proposes a pressure observer based adaptive dynamic surface controller (DSC). The pressure observer is used to predict the pressure at the inlet of the pneumatic cylinder and the long transmission lines are modeled as a nonlinear first order system. The DSC overcomes the problem of "explosion of complexity", which is often seen in techniques such a backstepping control. The results confirmed that the controller had good tracking performance and was robust to sudden disturbances.

Lastly, Smaoui et al. [26] proposed a backstepping controller for a pneumatic cylinder-type actuator. The concept of backstepping control involves designing controllers for individual subsystems and cascading the feedback signals back to the control input. The proposed controller demonstrates reduced static and position tracking errors compared to linear control techniques. However, it struggles in accurately identifying mass flow leakage and friction forces, which are significant factors in pneumatic systems.

Hybrid

Some controllers combined linear and non-linear techniques together as was observed in Figure 39, one of these control design as described by Koo lee et al [14], uses PID control in cascade with both position and pressure loops for a pneumatic cylinder type actuator. The pressure loop regulates the differential pressure in the cylinder, while the outer loop includes friction compensation. Friction compensation was generated though either a multi-layered perceptron type neural network or a reduced-order nonlinear observer. The result showed that including a friction model into the feedback linearization improved the tracking error significantly.

A different technique for predicting friction is proposed by Choux et al [28], where a cascade controller with a pressure and position loop is implemented for a hydraulic cylinder type actuator. The control architecture uses a backstepping approach together with a dynamic friction (LuGre) model to obtain the desired pressure difference between the two chambers. The proposed controller shows great improvement in position tracking when compared to a similar controller without the cascade structure [29].

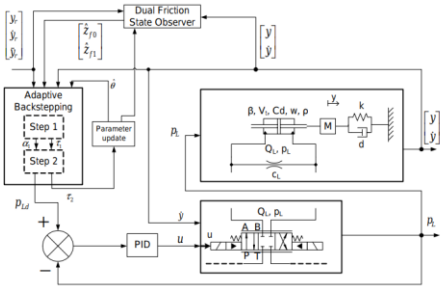

(a) Choux et al, Adapted from [28]

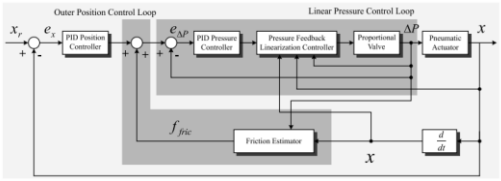

(b) Koo lee et al. Adapted from [14]

Figure 39 Hybrid control schemes

10.2. Appendix B: Feedback linearizable systems

To check whether a nonlinear system is feedback linearizable two conditions have to be met [20]. Suppose a nonlinear system is the following form

$$\dot{x} = f(x) + g(x)u. \tag{10.1}$$

Is feedback linearizable if the following controllability matrix

$$g = \left[g(x), ad_f g(x), \cdots, ad_f^{n-1} g(x)\right]. \tag{10.2}$$

has rank n. Where $ad_f g(x), \cdots, ad_f^{n-1} g(x)$ are the Lie brackets defined as

$$ad_f g(x) = \frac{\partial g}{\partial x} f(x) - \frac{\partial f}{\partial x} g(x) \tag{10.3}$$

$$ad_f^{n-1} g(x) = \frac{\partial ad_f^{n-2} g(x)}{\partial x} f(x) - \frac{\partial f}{\partial x} ad_f^{n-2} g(x).$$

The second condition that has to be met is the involutivity condition

$$D = span\left(g(x), ad_f g(x), \cdots, ad_f^{n-2} g(x)\right). \tag{10.4}$$

10.3. Appendix C: Lie derivatives

This appendix shows the Lie derivatives for the positive direction and are only valid if the velocity $x_2 > 0$. The derivatives are calculated with the symbolic math toolbox in MATLAB. The definition of the variables is explained in chapter 2.

$$L_{g1}h_1(x) = L_{g1}L_f h_1(x) = L_{g1}L_f^2 h_1(x) = 0 \tag{10.5}$$

The fourth Lie derivative of the input vector is

$$L_{g1}L_f^3 h_1(x) = \sqrt{2}A_p^2 A_v D_{ia} C_d x_3 x_4 * \frac{\sqrt{\left(\frac{2P_{in} - 2x_4}{2\rho_{x_4}}\right)}}{2IV_l V_{valve}\rho_{x_3} 2\left(\frac{1}{\rho_{x3}} - \frac{1}{\rho_{x4}} + \frac{f d_{x3}\left(L + L_{eqv}\right)}{4D_h\rho_{x3}}\right)}\dot{m}_{x_3}. \tag{10.6}$$

Where the vane motor inlet mass flow rate is defined as

$$\dot{m}_{x_3} = \sqrt{\frac{(x_4 - x_3)A_p^2}{\frac{1}{\rho_{x_3}} - \frac{1}{\rho_{x_4}} + f d_{x_3}\frac{L + L_{eqv}}{4\rho_{x_3}D_h}}}. \tag{10.7}$$

The Lie derivatives of the state vector for $x_2 > 0$ are

$$L_f h_1 = x_2 \tag{10.8}$$

$$L_f^2 h_1 = \frac{(x_3)D_{ia} - \tau_{stat} - \tau_{dyn}x_2 - \tau_{dyn2}x_2^2}{I}$$

$$L_f^3 h_1 = \frac{\left(\tau_{dyn} + 2\tau_{dyn2}x_2\right) * \left(\tau_{dyn2}x_2^2 + \tau_{stat}x_2 + \tau_{stat} - D_{ia}x_3\right)}{I^2} - \frac{D_{ia}x_3}{IV_l\rho_{x3}} * t3$$

$$L_f^4 h_1 = \left(x_3\frac{(t1 + t2)}{IV_l\rho_{x3}}\right)t3 - \frac{(t4 * t5)}{I} - t6.$$

With $t1$, $t2$, $t3$, $t4$, $t5$, and $t6$ defined as

$$t1 = \frac{D_{ia}\left(\tau_{dyn} + 2\tau_{dyn2}x_2\right)}{I^2} + \frac{\left(D_{ia}\left(V_{loss}x_3 - \dot{m}_{x_3} + D_{ia}\rho_{x3}x_2\right)\right)}{IV_l\rho_{x3}} \tag{10.9}$$

$$t2 = \left(D_{ia}x_3\left(V_{loss} + \frac{A_p^2}{2\left(\frac{1}{\rho_{x3}} - \frac{1}{\rho_{x4}} + \frac{f d_{x3}(L + L_{eqv})}{4D_h\rho_{x3}}\right)}\dot{m}_{x_3}\right)\right)$$

$$t3 = \frac{\left(V_{loss}x_3 - \dot{m}_{x_3} + D_{ia}\rho_{x3}x_3\right)}{IV_l\rho_{x3}}$$

$$t4 = \frac{\left(\tau_{dyn1} + 2\tau_{dyn2}x_2\right)^2}{I^2} + \frac{\left(2\tau_{dyn2}\left(2\tau_{dyn2}x_2^2 + \tau_{dyn1}x_2 + \tau_{stat} - D_{ia}x_3\right)\right)}{I^2} - \frac{D_{ia}^2 x_3(x_2 + x_2)}{2IV_l x_2}$$

$$t5 = \left(2\tau_{dyn2}x_2^2 + \tau_{dyn1}x_2 + \tau_{stat} - D_{ia}x_3\right)$$

$$t6 = \frac{A_p^2 D_{ia}x_3x_4}{2IV_l V_{valve}\rho_{x3}\rho_{x4}\left(\frac{1}{\rho_{x3}} - \frac{1}{\rho_{x4}} + \frac{f d_{x3}(L + L_{eqv})}{4D_h\rho_{x3}}\right)}.$$